Preliminary 3-D site-scale studies of radioactive colloid transport in the unsaturated zone at Yucca Mountain, Nevada

G.J. Moridis *, Q. Hu, Y.-S. Wu, G.S. Bodvarsson

Earth Sciences Division, Lawrence Berkeley National Laboratory, 1 Cyclotron Road, Berkeley, CA 94720, USA

Abstract

The U.S. Department of Energy (DOE) is actively investigating the technical feasibility of permanent disposal of high-level nuclear waste in a repository to be situated in the unsaturated zone (UZ) at Yucca Mountain (YM), Nevada. In this study we investigate, by means of numerical simulation, the transport of radioactive colloids under ambient conditions from the potential repository horizon to the water table. The site hydrology and the effects of the spatial distribution of hydraulic and transport properties in the Yucca Mountain subsurface are considered. The study of migration and retardation of colloids accounts for the complex processes in the unsaturated zone of Yucca Mountain, and includes advection, diffusion, hydrodynamic dispersion, kinetic colloid filtration, colloid straining, and radioactive decay. The results of the study indicate that the most important factors affecting colloid transport are the subsurface geology and site hydrology, i.e., the presence of faults (they dominate and control transport), fractures (the main migration pathways), and the relative distribution of zeolitic and vitric tuffs. The transport of colloids is strongly influenced by their size (as it affects diffusion into the matrix, straining at hydrogeologic unit interfaces, and transport velocity) and by the parameters of the kinetic-filtration model used for the simulations. Arrival times at the water table decrease with an increasing colloid size because of smaller diffusion, increased straining, and higher transport velocities. The importance of diffusion as a retardation mechanism increases with a decreasing colloid size, but appears to be minimal in large colloids.
 Published by Elsevier Science B.V.

Keywords: Yucca Mountain; Vadose zone; Radioactive colloid transport; Numerical modeling

---

* Corresponding author.
 E-mail address: gjmoridis@lbl.gov (G.J. Moridis).

1. Introduction

1.1. Background

The U.S. Department of Energy (DOE) is actively investigating the technical feasibility of permanent disposal of high-level nuclear waste in a repository to be situated in the unsaturated zone (UZ) at Yucca Mountain (YM), Nevada. The potential site is located in southern Nevada about 120 km northwest of Las Vegas. The attractive attributes of the site include a semi-arid climate with an average rainfall of about 170–190 mm/year (indicating low infiltration rates through the potential repository), a thick UZ (600–700 m), the presence of rocks onto which important radionuclides in the wastes sorb strongly, and the relative isolation and sparse population of the proposed area.

The YM stratigraphy consists of layers of welded and nonwelded tuffs with vastly different hydraulic properties (Montazer and Wilson, 1984; Liu et al., 1998). The location of the potential repository is approximately 300 m below the surface, i.e., at the midpoint between the surface and the water table (Dyer and Voegele, 1996). A substantial body of work on the characterization and modeling of geology, hydrology, and geochemistry of the site is available. Interested readers are directed to the studies of Montazer and Wilson (1984), Buesch et al. (1995), Ahlers et al. (1999), Dyer and Voegele (1996), Bodvarsson et al. (1999), Bandurraga and Bodvarsson (1999), Doughty (1999), Wu et al. (1999a,b), Sonnenthal and Bodvarsson (1999), Haukwa et al. (1999), Wang et al. (1999), and Birkholzer et al. (1999) for a review of the current status of knowledge on these subjects.

1.2. Purpose of the study

The purpose of this study is to evaluate by means of 3-D numerical modeling the transport of radioactive colloids in the UZ from the potential repository to the water table under ambient conditions. The model considers the transport of radioactive colloids through fractured tuffs, and the effects of the fracture characteristics in the various hydrogeologic units. It accounts for advection, diffusion, hydrodynamic dispersion, kinetic filtration, straining and radioactive decay.

The simulations of colloid transport from the repository horizon to the water table are performed to support model development and support studies for performance assessment. The results of the simulations are used to determine the relative importance of processes, mechanisms, and geologic features that significantly affect transport.

The primary caveat for using the modeling results documented here is that the input transport parameters were based on limited site data. For some input parameters, best estimates were used because no specific data were available. An additional caveat is that the colloid transport model is based on the conceptual models and numerical approaches used for developing the flow fields and infiltration maps (Wu et al., 2000), and thus they share the same limitations.

2. Geological model and physical processes

2.1. Geological system

The subsurface formations at YM consists of heterogeneous layers of anisotropic, fractured volcanic rocks. There are alternating layers of welded and nonwelded ash flow and air fall tuffs. The cooling history of these volcanic rock units determines their mechanical and hydrologic properties. Beginning from the land surface downward, the YM geologic units are the Tiva Canyon, Yucca Mountain, Pah Canyon, and the Topopah Spring Tuffs of the Paintbrush Group. Underlying these are the Calico Hills Formation, and the Prow Pass, Bullfrog, and Tram Tuffs of the Crater Flat Group. These formations have been divided into major hydrogeologic units based roughly on the degree of welding. These are the Tiva Canyon welded (TCw); the Paintbrush nonwelded (PTn), consisting primarily of the Yucca Mountain and Pah Canyon members and the interbedded tuffs; the Topopah Spring welded (TSw); the Calico Hills nonwelded (CHn); and the Crater Flat undifferentiated (CFu) hydrogeologic units (Bodvarsson et al., 1999; Hinds and Pan, 2000).

Conceptual models of flow at YM are described in Liu et al. (2000). In the present study, we focus on the subject of colloid transport in the hydrogeologic units beneath the potential repository horizon. The potential repository will reside in the TSw unit (McKenzie, 1999), and more specifically the tsw34, tsw35, and tsw36 layers of the UZ, depending on the location (Hinds and Pan, 2000; Liu et al., 2000). A schematic of the UZ, its hydrogeologic units, and the site of the potential repository are shown in Fig. 1.

Unsaturated flow in the TSw is primarily through the fractures, because the matrix permeability in many of the TSw layers can support flows of only a few millimeters per year. The average fracture spacing in the TSw layers is about 0.5 m (Liu et al., 2000; Bodvarsson et al., 1999). The CHn and the Prow Pass (PP) unit below the potential repository horizon are complex geological systems with highly heterogeneous distributions of fracture and matrix hydrological properties. The distribution of these properties is expected to have a pronounced effect on the transport of radionuclides in the UZ. There is limited hydrologic and transport information on the CHn unit and even less on the PP. The permeability of nonwelded tuffs is strongly dependent on the degree of alteration of the rock minerals into zeolites. Zeolitic alteration in the CHn (a common occurrence in its lower layers) can decrease the matrix permeability by orders of magnitude in relation to that of the welded tuffs (Liu et al., 2000). In nonwelded vitric tuffs, the matrix and fracture permeabilities are on the same order of magnitude (Liu et al., 2000). Thus, these layers behave as porous (rather than fractured) media, and flow is matrix-dominated. This has important implications for transport because of the longer contact times in these non-welded tuff units.

The CHn major hydrogeologic unit is composed of vitric (CHv) and zeolitic (CHz) units (Hinds and Pan, 2000). Typically, radionuclides are more strongly adsorbed onto zeolitic units than onto vitric units. Flow in the CHz units is expected to be concentrated in the fractures because of the low CHz fracture density (compared to the TSw) and the large permeability contrast between matrix and fractures (Liu et al., 2000): permeability in the
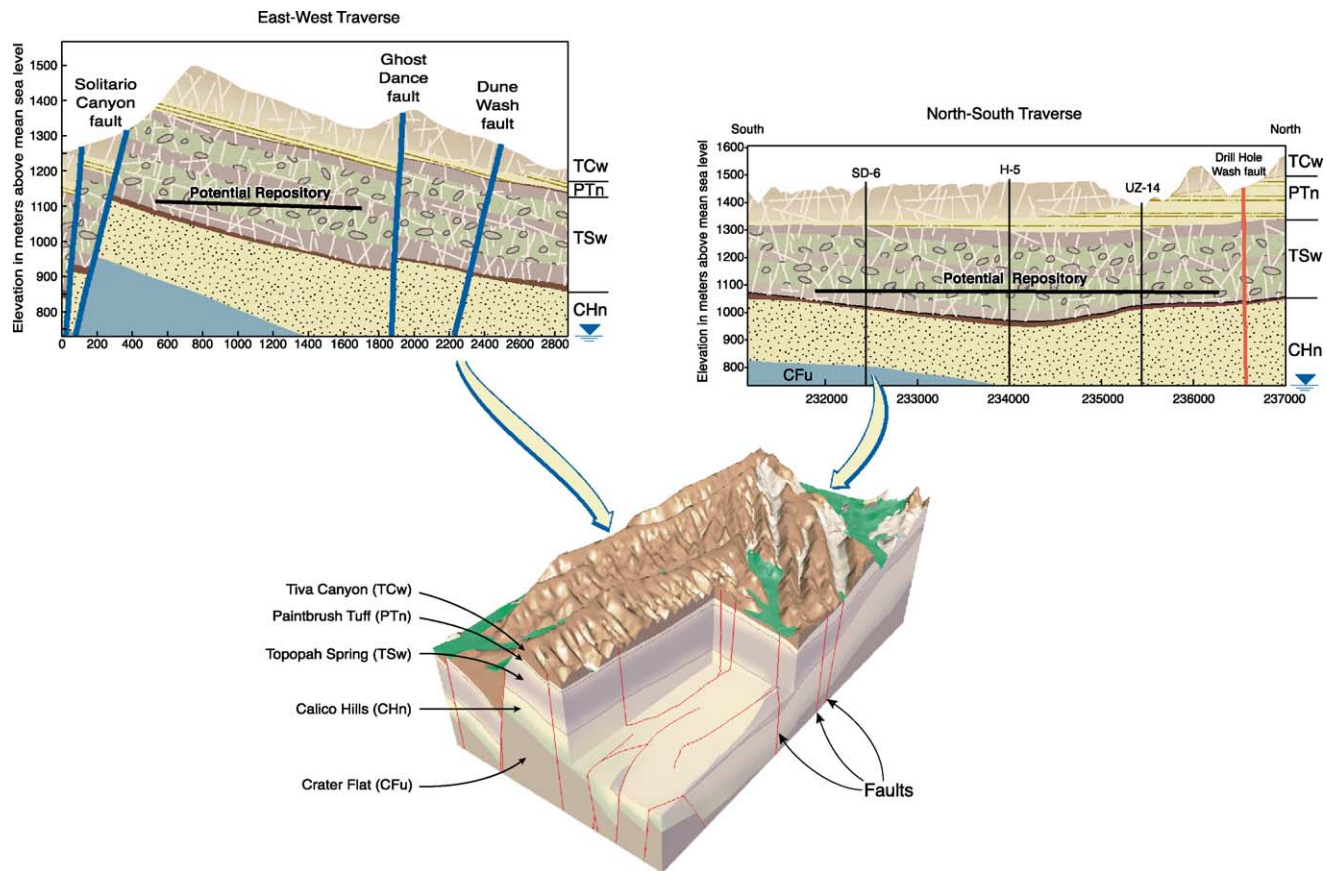
Fig. 1. A schematic of the UZ system and of the potential repository (Wu et al., 2000).

fractures is about five orders of magnitude larger than in the matrix. Fracture-dominated flow is associated with short contact times, limited radionuclide removal through diffusion and sorption, and thus transport over longer distances.

2.2. Transport

Radioactive contaminants can escape from the waste stored in the potential repository. These contaminants can migrate through the UZ of YM as dissolved molecular species or in colloidal form. Transport of these radioactive solutes or colloids involves advection, hydrodynamic dispersion, sorption (solutes) or filtration (colloids), matrix diffusion, and radioactive decay. The transport of radionuclides is also affected by factors such as solubility limits, the presence of perched water, and heating effects from the potential repository. In this section we briefly discuss the phenomena, processes, and factors affecting transport.

2.2.1. Advection

In YM, flow is predominately downward (in response to gravitational differentials), and so is advective transport (DOE, 1998). Some lateral advection is also expected in response to lateral flow diversion at the boundaries of hydrogeologic units with sharp contacts in their hydraulic properties. Such diversion occurs in the perched water bodies of the UZ (Wu et al., 2000). Laterally diverted flow ultimately finds a pathway to the water table through other, more permeable zones (e.g., faults).

Advection in the fractures is expected to be the dominant transport mechanism in many layers of the various hydrogeologic units. This is because the expected flow rates (based on estimates of areal averages of deep percolation rates) exceed those that can be supported by the rock matrix permeability. This leads inevitably to flow focusing in the more permeable fractures. Advection is the dominant transport mechanism in the fractures because of high permeability, limited fracture pore volumes, limited contact area, and short contact times between the radionuclide-carrying liquid phase and the matrix (only at the fracture walls). In a few hydrogeologic units, such as the CHv, matrix flow is dominant, resulting in much slower transport velocities (compared to those in the fractures of other units), and longer contact times of the radionuclides with the matrix (DOE, 1998).

2.2.2. Hydrodynamic dispersion

There is practically no information on colloidal dispersion in the various hydrogeologic units of the UZ. However, dispersion is not expected to play a significant role in the transport of radionuclides in the fractures (and is not considered in this study) because of the predominant role of advection as the main transport mechanism.

2.2.3. Matrix diffusion

Diffusion can play an important role in radionuclide exchange between the fractures and the rock matrix. This process transfers radioactive colloids into the matrix (where water flow is slow and filtration occurs), thus removing them from (and slowing their advance in) the fast fracture flow. Diffusive flux across an interface is a function of the concentration gradient, the temperature, the size of the dissolved species and its electric

charge, the matrix pore structure, and the water saturation (DOE, 1998). Colloidal diffusion is normally limited because of their relatively large size (compared to solutes).

2.3. Colloids

The generation and mobilization of colloids in the UZ of YM are considered important issues in the transport of radioactive true (intrinsic) colloids (e.g., colloidal Pu(IV) and Pu(V)) and the colloid-assisted transport of radioactive species sorbed on pseudocolloids (e.g., naturally occurring clay colloids). Such species can include ^{239}Pu, ^{237}Np, ^{243}Am, and ^{247}Cm in high-level radionuclide wastes, or ^{137}Cs, ^{90}Sr, and ^{60}Co in low-level radioactive wastes (Conca, 2000).

2.3.1. Colloidal behavior

Colloids are very fine particles (such as clay minerals, metal oxides, viruses, bacteria, and organic macromolecules) that range in size between 1 and 1000 nm (McCarthy and Zachara, 1989) and have high, size-dependent, specific surface areas. Their chemical behavior is dominated by surface processes (EPRI, 1999), and can have a high sorptive capacity for contaminants. Colloids are deposited on porous and fractured media by surface filtration, straining filtration, and physical–chemical filtration. Colloid transport differs from solute transport because the colloidal particle interactions (e.g., flocculation), mechanical clogging effects, and surface reactions (e.g., deposition or attachment) are substantially different from solute processes and phenomena.

Radioactive true colloids or radionuclides adsorbed onto pseudocolloids can be transported over significant distances (McCarthy and Zachara, 1989). The significant migration of strongly sorbing Pu and Am (more than 30 m) from a low-level waste site at Los Alamos National Laboratory through unsaturated tuff over a period of approximately 30 years is attributed to colloid and/or colloid-assisted transport, a hypothesis confirmed by laboratory experiments (Buddemeier and Hunt, 1988). Kersting et al. (1999) demonstrated that the soluble (ionic) Pu is practically immobile in the subsurface of the Nevada Test Site (NTS) because of its strong sorption and limited solubility, but can be transported over significant distances (1.3 km over a 30-year period) in a colloidal form.

Colloid attachment to the host rock is strongly dependent on electrostatic interactions. Colloid detachment (declogging) is generally slow to irreversible. Sorption of radionuclides on colloids is controlled by a range of chemical processes such as ion exchange, surface complexation, and organic complexation (EPRI, 1999), and can be very strong. This may decrease the concentration of strongly sorbing solute radionuclides (e.g., ^{239}Pu) but may increase the concentration of radioactive colloids in the liquid phase in the fractures and the matrix of the UZ layers.

2.3.2. Colloid migration in macroporous and fractured systems

In laboratory experiments, Jacobsen et al. (1997) observed significant transport of clay and silt colloid particles through macropores. Macropores can facilitate the transport of colloids because all types of filtration are less pronounced in large pores and the higher water velocities can lead to increased detachment (as the hydrodynamic forces can overcome the colloid–grain bonding forces).

In a study of colloid-facilitated transport of radionuclides through fractured media, Smith and Degueldre (1993) determined that radionuclide sorption onto colloids is effectively an irreversible process. Such radionuclide-laden colloids can migrate over long distances in macropores and fractures, and, being much larger than solutes, they exhibit little retardation because their size prevents them from entering the wall-rock pores. Vilks and Bachinski (1996) studied particle migration and conservative tracer transport in a natural fracture, and observed that the conservative tracer lagged slightly behind the colloid front, but colloid mobility was significantly reduced when the average groundwater velocity decreased. Compared to dissolved tracers, the migration of colloids was more affected by the flow path and flow direction. This tendency can have a significant effect in the fracture-dominated flow of the UZ in the YM system.

Vilks et al. (1997) conducted a field-scale colloid migration experiment under induced flow conditions using silica colloids in a fractured medium. Their analysis suggested that although colloid migration appeared to behave conservatively, colloids may have followed different pathways than dissolved conservative tracers.

2.4. Colloid filtration

Filtration is one of the main mechanisms of radioactive colloid removal from the transporting liquid phase. Two types of filtration mechanisms are considered in this study: straining filtration and physical–chemical filtration.

2.4.1. Straining filtration

There are two types of straining: (a) conventional straining, when the colloid is larger than the pore throat diameter or the fracture–aperture width (Herzig et al., 1970), and (b) film straining, when the colloid is larger than the thickness of the adsorbed water film coating the grains of the rock (Wan and Tokunaga, 1997).

Only conventional straining is considered in this study, and is hereafter referred to as straining or pore-size exclusion. Such filtration is determined by the ratio $R_d = d_g/d_p$ (where d_g is the diameter of the grains of the porous medium and d_p is the colloid diameter), and practically ceases when $R_d > 12$ (Herzig et al., 1970).

2.4.2. Physical–chemical filtration

In this study, references to filtration are implied to indicate physical–chemical filtration. This type of filtration type incorporates (a) contact with the pore walls, (b) colloid fixation onto the walls, and (c) release of previously fixed colloids (Herzig et al., 1970; Çorapçioglu et al., 1987).

Contact with the pore walls and colloidal capture can be the result of sedimentation, inertia, hydrodynamic effects, direct interception and diffusion. Fixation on the pore walls occurs at favorable retention sites, and is caused by forces that include axial pressure of the fluid at constriction sites, friction forces, van der Waals forces, electrical forces and chemical forces (Herzig et al., 1970). Remobilization of colloidal particles may be caused by a number of factors, including collision between a loosely held colloid with a moving particle, an increase in pressure as colloids constrict flow, and a change in external conditions.

2.5. Colloids at Yucca Mountain

The available data on colloid occurrence and concentrations at the YM site are limited and pertain to saturated zone studies. No information has been published on colloids in the unsaturated zone. The current state of understanding is that (a) the natural colloid concentrations in native waters at the YM site are low ($10^6 - 10^{10}$ particles/ml), and (b) waste-form colloids will be the dominant colloidal species of concern to transport studies (McGraw, 2000).

Additional information from nearby sites, however, cannot be ignored. Preliminary results of a groundwater survey from the NTS have shown that the Pahute Mesa drainage waters (both on and off the NTS) have colloid loadings of 0.8–6.9 mg/l. Such relatively high concentrations can explain the observed transport of strongly sorbing radionuclides over significant distances, particularly because the ionic composition of the NTS ground-water does not promote the coagulation of clay colloids (Buddemeier and Hunt, 1988). This is because NTS groundwater is low in organic matter, and a substantial fraction of the colloidal material is composed of stable natural minerals.

In addition to natural colloids, anthropogenic colloids may be created from the waste itself or from repository construction and sealing materials. Waste- and repository-derived colloids at Yucca Mountain are likely to include organic colloids, iron oxyhydroxides, and aluminosilicate colloids (EPRI, 1999). In a 50-month experiment involving simulated weathering of a high-level nuclear waste glass, spallation and nucleation were identified as the main mechanisms of colloid genesis (Bates et al., 1992). The same study determined that Pu and Am released from waste were predominantly in the colloidal, rather than in the dissolved, form.

2.6. Important points for consideration in colloid transport

The assessment of the potential role of colloids in the transport of radionuclides at YM is particularly challenging for the reasons discussed in the previous sections and is further complicated by the following factors.

(1) Different types of colloids (minerals, organics, microbes, and polymeric actinide colloids) with substantially different characteristics and properties (e.g., hydrophobicity and surface charges) that strongly affect their behavior in the subsurface.

(2) Colloid generation, growth, stability, size distribution, and concentration are dynamic. Knowledge of the temporal and spatial distributions of colloid populations in the different hydrogeologic units is difficult to obtain. Changes in the ionic strength of the aqueous solution (e.g., when percolating water in an episodic infiltration event encounters resident pore water) can affect colloid stability. There are also uncertainties about the colloid stability in the aqueous phase of the UZ and about the colloid generation from mineral-coated fracture walls (given the predominance of fracture flow in the UZ).

(3) Measurements of colloid concentration in the unsaturated zone are difficult. Because of low concentrations and low saturations in the UZ, the determination of colloid concentration in pore water is challenging, and serious questions arise about sample representativity and integrity.

(4) The concentration of waste-form colloids is a key uncertainty. There is evidence to suggest that the low concentration of natural colloids in the UZ of YM will not lead to significant colloid-assisted transport and that waste-form colloids will be the dominant colloidal transport problem (McGraw, 2000). Thus, there is a need for reliable estimates of the types and generation rates of waste-form colloids, subjects on which there is considerable uncertainty (EPRI, 1999).

3. 3-D site-scale simulations of radioactive colloid transport

3.1. The EOS9nT code

The code used for the 3-D site-scale transport simulations in the study is TOUGH2 (Pruess, 1991) with the EOS9nT module (Moridis et al., 1999). It can simulate flow and transport of an arbitrary number n of nonvolatile tracers (solutes and/or colloids) in the subsurface.

EOS9nT first solves the Richards equation, which describes saturated or unsaturated water flow in subsurface formations, and obtains the flow regime. The set of n independent transport equations (corresponding to the n solutes/colloids) are then solved sequentially. The n tracer transport equations account for (i) advection, (ii) molecular diffusion, (iii) hydrodynamic dispersion (with full 3-D tensorial representation), (iv) kinetic or equilibrium physical and chemical sorption (linear, Langmuir, Freundlich, or combined), (v) first-order linear chemical reaction, (vi) radioactive decay, (vii) pore-size exclusion, (viii) filtration (equilibrium, kinetic or combined), and (ix) colloid-assisted solute transport. A total of $n - 1$ daughters of radioactive decay can be tracked.

EOS9nT includes two types of Laplace transform formulations of the tracer equations, in addition to conventional timesteping. The Laplace transform is applicable to steady-state flow fields and allows a practically unlimited time step size and more accurate solution (as numerical diffusion is significantly reduced). Additional information on the EOS9nT numerical model can be found in Moridis et al. (1999).

3.2. The simulation process

3.2.1. Flow simulations

The simulations proceeded in two parts. In the first part, only the flow (Richards) equation was solved to obtain the steady-state flow field in the 3-D domain of the UZ of YM. This was done to exploit the capabilities of the EOS9nT code (Moridis et al., 1999), which can produce very fast and efficient solutions of large 3-D systems when the flow fields are known.

For the study of radionuclide transport, the steady-state flow field was obtained assuming an invariant present-day infiltration regime. This corresponds to an average percolation flux of 4.6 mm/year, as determined by Hevesi and Flint (2000). The grid, conditions and properties of the simulated geologic system were those of the fully calibrated UZ model of Wu et al. (2000), and corresponded to the #1 conceptual model of perched water. This is the permeability barrier model, which uses the calibrated perched

water parameters for fractures and matrix in the northern part of the model domain, and modified property layers (including the tsw38, tsw39, ch1z and ch2z layers) where the lower basal vitrophyre of the TSw is above the CHn zeolites.

3.2.2. Transport simulations

The steady-state flow field for a mean present-day infiltration and the #1 perched water model was the used as an input for all the 3-D colloid transport simulations. The parameters used in the EOS9nT simulations of 3-D transport of the colloids are listed in Table 1. A more detailed discussion of the input data can be found in Moridis et al. (2000) and Conca (2000).

All the simulations were conducted by using the De Hoog et al. (1982) implementation of the Laplace transform formulation of EOS9nT. This was selected because of the speed and accuracy of this formulation, its ability to provide information over the whole spectrum of the simulation period, and its ability to drastically reduce numerical diffusion. The resulting matrices were very well behaved, requiring no more that $10-15$ conjugate gradient iterations to reduce residuals to below the 10^{-11} level in a matrix of order of about 200,000. Thus, simulations were very fast, requiring $1800-2200$ s of execution time to cover a simulation period of 10^6 years.

3.2.3. Grids and boundary conditions

The grid used in the 3-D site-scale simulations consisted of about 100,000 elements and involved a dual-permeability scheme to describe the fractured geology in the UZ. The same grid was used for both the flow and the transport simulations (Moridis et al., 2000; Wu et al., 2000). A 2-D (plan) view of the grid at the potential repository level is shown in Fig. 2, which also shows important geologic features at the same level.

The time-invariant but spatially variable infiltration rate determined by (Hevesi and Flint, 2000) was applied to the top gridblocks of the 3-D domain. For the transport

Table 1
Input parameters for the EOS9nT 3-D site-scale simulations of colloid transport

| Parameters	Source
Tortuosity $\tau \simeq \phi$	Farrell and Reinhard (1994)
Longitudinal dispersivity $\alpha_L = 0.5$ m in the fractures, 0.05 m in the matrix	Scientific judgement in the absence of available data
Properties and characteristics of the geologic units, steady-state pressures, water saturations and flow fields	Clayton (2000)
Colloid density $\rho_c = 11,640$ kg/m^3 (PuO$_2$)	Lide (1992)
Half-life of ^{239}Pu $T_{1/2} = 2.41 \times 10^4$ years	Lide (1992)
Forward kinetic filtration (clogging) coefficient κ^+	Eqs. (2), (5) and (6), parameters computed at 25 °C
Backward (reverse) kinetic filtration (declogging) coefficient $\kappa^- = 100 \, \kappa^+$; $0.1 \, \kappa^+$; 0	Reasonable estimates bracketing the range of κ^-
Fracture porosity $\phi = 0.99$	A reasonable estimate that allows limited colloid filtration (attachment) in the fractures
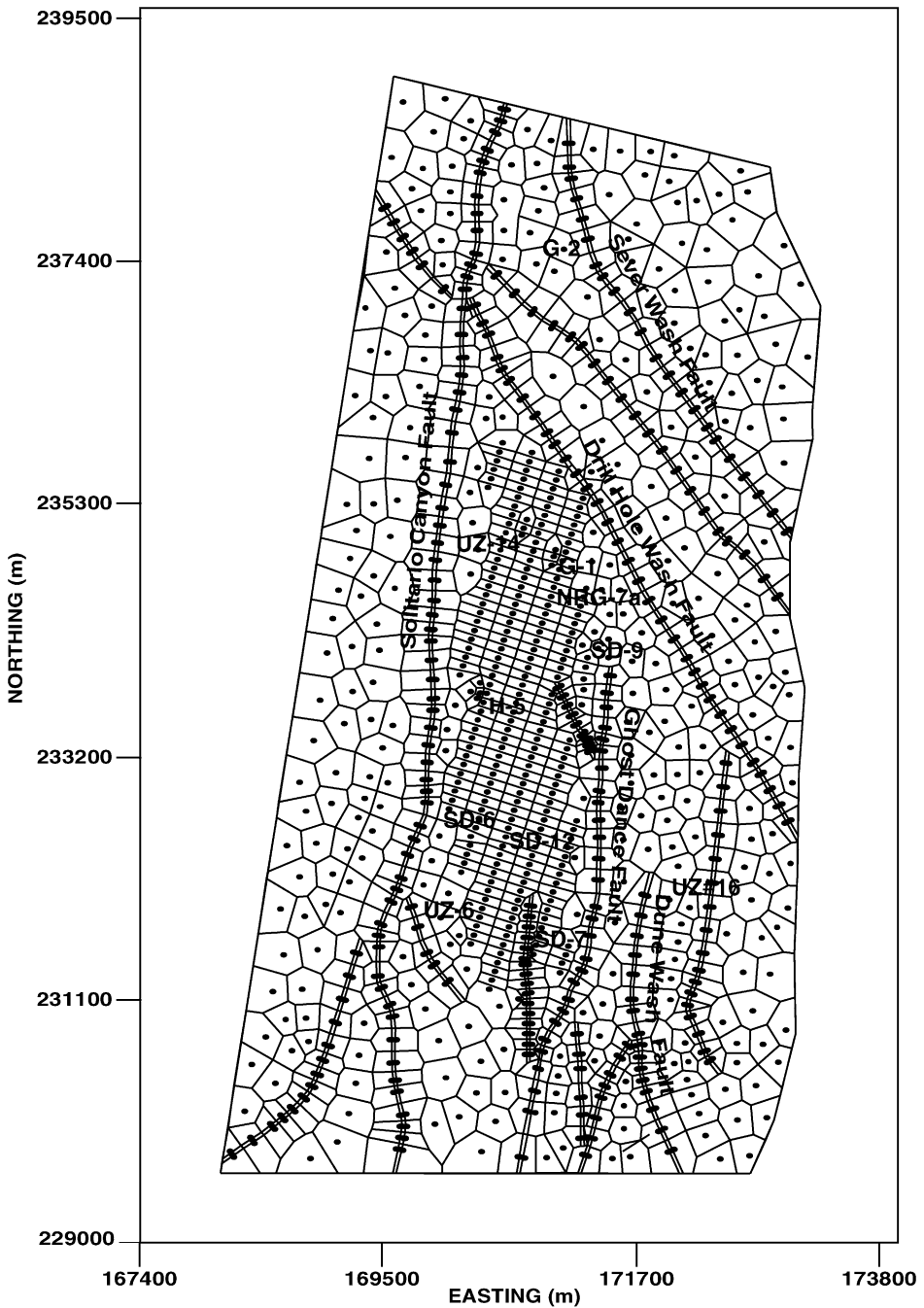
Fig. 2. Two-dimensional (plan) view of the UZ model grid design at the potential repository level (Hinds and Pan, 2000).

simulations, a time invariant and areally uniform constant concentration was imposed in the fractures of all the gridblocks immediately below the potential repository.

3.3. Colloid filtration model

The EOS9nT filtration option used in the colloid transport simulations is described by the linear kinetic model (Moridis et al., 1999),

$$\frac{\partial \sigma}{\partial t} = \kappa^+ X - \kappa^- \sigma, \tag{1}$$

where σ is the filtered concentration of the colloid expressed as volume of colloids per volume of the medium $[L^3 L^{-3}]$, X is the mass fraction of colloids in the aqueous phase $[M^1 M^{-1}]$, and κ^+ and κ^- $[T^{-1}]$ are the kinetic forward and reverse (or, clogging and declogging coefficients) colloid filtration coefficients, respectively, which are specific to each colloid and rock type. The term κ^- is commonly assumed to be zero (Bowen and Epstein, 1979), but there is insufficient evidence to support this. From de Marsily (1986) and Ibaraki and Sudicky (1995),

$$\kappa^+ = \epsilon f u G, \tag{2}$$

where ϵ is the filter coefficient of the porous medium $[L^{-1}]$, f is a velocity modification factor, u is the Darcy velocity $[LT^{-1}]$, and G is a dynamic blocking function (DBF) that describes the variation of the PM porosity and specific surface with σ (James and Chrysikopoulos, 1999). The factor f ($1 \leq f \leq 1.5$) accounts for the velocity of the colloidal particle flow being larger than that of water (Ibaraki and Sudicky, 1995). This results from the relatively large size of the colloids, which tends to concentrate them in the middle of the pores where the groundwater velocity is larger than the bulk average velocity. The factor f tends to increase with decreasing ionic strength, but cannot exceed 1.5 because colloids cannot move faster than the maximum groundwater velocity (Ibaraki and Sudicky, 1995). For the deep filtration conditions in the UZ of YM (because of very dilute colloidal suspensions), there is no interaction among the colloidal particles and no effects on the medium porosity and permeability, i.e., ϕ is constant, and $G = 1$.

3.4. Colloidal forms and properties

Because there are indications that colloid-assisted transport (i.e., transport by pseudo-colloids) in the UZ of YM will not be significant because of the low concentrations of naturally occurring colloids such as clays (McGraw, 2000), only true colloids were considered. Those were taken to have the properties of PuO_2 and the radioactive decay characteristics of the [239]Pu isotope. Note that the simulation results also apply to pseudo-colloids onto which [239]Pu has sorbed irreversibly.

Four colloids of different sizes were considered: 6, 100, 200 and 400 nm. Their sizes, velocity adjustment factors (f) and their accessibility factors (f_c, defined as the fraction of the colloid that is not strained and is allowed to enter a particular hydrogeologic unit) were taken from McGraw (2000), and are shown in Table 2. The colloidal diffusion coefficient

Table 2
Properties of the four colloids in the EOS9nT simulations

Parameter	450 nm	200 nm	100 nm	6 nm
Diffusion coefficient[a] D_0 (m^2/s)	9.53×10^{-13}	2.15×10^{-12}	4.29×10^{-12}	7.15×10^{-11}
Velocity adjustment factor[b] f	1.5	1.2	1.1	1.0
Accessibility factor[c] f_c in the TSw	0.05	0.10	0.20	0.75
Accessibility factor[c] f_c in the CHv	0.45	0.50	0.55	0.80
Accessibility factor[c] f_c in the CHz	0.20	0.25	0.25	0.65

[a] Eq. (3).
[b] Reasonable estimates.
[c] McGraw (2000).

D_0 $[L^2T^{-1}]$ is computed internally by EOS9nT (Moridis et al., 1999) using the Stokes–Einstein equation

$$D_0 = \frac{kT}{3\pi\mu_w d_p}, \tag{3}$$

where k is the Boltzmann constant, T is the absolute water temperature $[K]$, μ_w is the dynamic viscosity of water $[ML^{-1}T^{-1}]$, and d_p is the colloid diameter $[L]$.

The effective diffusion coefficient D_e is computed as

$$D_e = \phi\tau S_w D_0 \tag{4}$$

where ϕ is the porosity $[L^3L^{-3}]$, τ (≤ 1) is the tortuosity factor $[L^1L^{-1}]$ and S_w is the water saturation $[L^3L^{-3}]$. In this study, $\tau \simeq \phi$, an approximation supported by experimental evidence (Farrell and Reinhard, 1994; Hu and Brusseau, 1995; Grathwohl, 1998). The work of Conca and Wright (1990) on solutes suggested that the dependence of S_w on D_e is stronger than the linear relationship of Eq. (4). This subject merits additional attention because of its potential implications in colloid transport. The linear relationship assumed in this study results in increased transport estimates because diffusion from the fractures into the matrix is reduced.

3.5. Colloid filtration coefficients

Pore-size exclusion (straining filtration) was described using the accessibility factors shown in Table 2. The forward kinetic coefficient κ^+ was computed from Eq. (2), in which the velocity coefficients are as shown in Table 2, and ϵ is computed from Yao et al. (1971) as

$$\epsilon = 1.5\frac{1-\phi}{d_m}\alpha_c\eta_c, \tag{5}$$

where d_m is the particle size of the medium grains or the fracture aperture $[L]$, α_c is the single collector efficiency,

$$\eta_c = 0.9\left(\frac{k_B T}{\mu_w d_c d_m u}\right)^{2/3} + 1.5\left(\frac{d_c}{d_m}\right)^2 + (\rho_c - \rho)\frac{g d_c^2}{18\mu u} \tag{6}$$

k_B is the Boltzman constant, d_c is the colloid diameter $[L]$, T is the absolute temperature, and all other terms remain as previously defined. The clogging (forward) kinetic coefficients κ^+ are computed internally in EOS9nT.

3.6. The colloid transport simulation cases

No information exists on the kinetic declogging (reverse) coefficient κ^-. To alleviate the problem, we treated κ^- in the EOS9nT simulations as a fraction of κ^+. We believe that this is a better approach than using a constant κ^- assumption because it maintains dependence on the flow velocity. The following four cases were investigated:

(1) $\kappa^- = 0$. This corresponds to a case of no declogging, in which colloids, once filtered, do not detach from the pore/fracture walls.

(2) $\kappa^-/\kappa^+ = 100$. This corresponds to strong kinetic declogging and will provide an estimate of maximum colloidal transport (the worst-case scenario).

(3) $\kappa^-/\kappa^+ = 0.1$. This corresponds to weak kinetic declogging and approximates a mild equilibrium filtration behavior.

(4) Same as in Case 2, but the fractures are assumed to have the same colloidal transport properties as the corresponding matrix. This study provides an estimate of the importance of fractures in the transport of colloids. Note that the change in the filtration properties affects only 1% of the fracture pore volume (because $\phi = 0.99$ in the fractures; see Table 1 and Eq. (4)).

4. Results and discussion

4.1. Uncertainties, assumptions and limitations

To our knowledge, this is the first formal attempt to study 3-D site-scale radioactive colloid transport in the UZ of YM. While the results presented in this section provide some elucidation of colloid transport, caution should be exercised in their interpretation. This is because of the conceptual approach and assumptions of this study, and the substantial knowledge gaps in the area of colloid behavior.

It is important to keep in mind that this study uses relative quantities (with respect to the colloid concentration in the water released from the potential repository), and, consequently, all the concentration predictions are relative in nature and presuppose the ability (by no means guaranteed) of the radioactive colloids to reach the underlying fractures. Thus, predictions of large relative concentrations may mean little unless and until the colloid release becomes possible, significant and known. Moreover, the presented analysis assumes that conditions for the creation and stability of colloids exist, and that the effects of the near-field chemical, physical, mineralogical and thermal conditions on their creation and stability over time can be ignored. While these assumptions may provide a worst-case scenario, they may be unrealistically conservative.

Note that the 3-D site-scale simulations discussed here do not describe a realistic (expected case) scenario: radioactive colloid release is assumed to occur continuously, uniformly and at a constant concentration over time and over the whole area of the potential

repository. This presupposes the near-simultaneous rupture of all the waste-containing vessels, the ability of water dripping into the potential repository to focus exclusively on the ruptured vessels and to flow through them, the spatially and temporally constant contaminant release from each waste package, and the lack of any colloid-destabilization process before they enter the fractures. The geologic model used in the analysis involves continuous fracture-to-fracture flow in certain portions of the UZ, greatly facilitating transport from the potential repository to the groundwater. While these assumptions provide the upper limit of a worst-case scenario, this is an implausible (if not a virtually impossible) situation. In that respect, the results discussed here should be viewed as an attempt to identify and evaluate the mechanisms, processes and geological features that control colloid transport using the largest possible input signal (i.e., the worst-case scenario) rather than as an effort to quantitatively predict the effects of a realistic colloid release regime.

There are significant uncertainties in colloid modeling (see Section 2). The currently available kinetics models were developed from theoretical principles (Herzig et al., 1970; Yao et al., 1971), and were tested under saturated conditions in uniform sandy laboratory experiments (van de Weerd and Leijnse, 1997) and small-scale field tests (Harvey and Garabedian, 1991) that involved microspheres or bacteria. It is not known if these models are applicable to the unsaturated complex fracture–matrix system and the expected colloidal waste forms in the UZ of YM.

The limitations of the equations predicting κ^+ have not been tested under the UZ conditions, and the subject of κ^- has barely been raised. The tremendous variation in behavior with the change in the kinetic declogging coefficient κ^- indicates the sensitivity of transport to the largely unknown κ^-. The sensitivity of the model to these parameters is evidenced by the change in t_{10} (defined as the time at which the normalized release rate $R = 0.1$) of the larger colloids from 15 years to about 12,000 years to infinity as the value of κ^- changes from 100 κ^+ (fast declogging) to 0.1 κ^+ (slow declogging) to 0 (no declogging). Thus, the change in transport behavior with a changing κ^- should be viewed as indicative and qualitative, rather than quantitative and predictive.

4.2. Colloid transport in Case 1

The results of this simulation indicate no colloid breakthrough at any time either at the bottom of TSw unit or at the water table. This is consistent with the underlying clogging-only model.

4.3. Colloid transport in Case 2

4.3.1. Breakthrough curves in Case 2

Because the colloidal concentrations in the potential repository and in the bottom boundary elements (corresponding to the water table) remain constant over time in our model, the breakthrough concept was based on the normalized release rate R, which is defined as

$$R = \frac{\text{Mass release rate at the groundwater boundary } [MT^{-1}]}{\text{Mass release rate at the potential repository } [MT^{-1}]}$$

Note that the term R is relative, and these findings are only important if the magnitude of the release rate at the potential repository becomes significant.

Fig. 3 shows the relative release rate R of the four colloids at the water table. Two observations appear particularly important. The first is the very fast breakthrough of the larger colloids (characterized by a rapid rise of the breakthrough curve), the rapidity of which increased slightly with the colloid size. The t_{10} for the three larger colloids is only about 15 and 30 years for the 6 nm colloid; t_{50} (defined as the time at which $R = 0.5$) is about 60 years for the 450 and 200 nm colloid, about 80 years for the 100 nm colloid, and 1200 years for the 6 nm colloid. The second observation is that, counter to expectations,
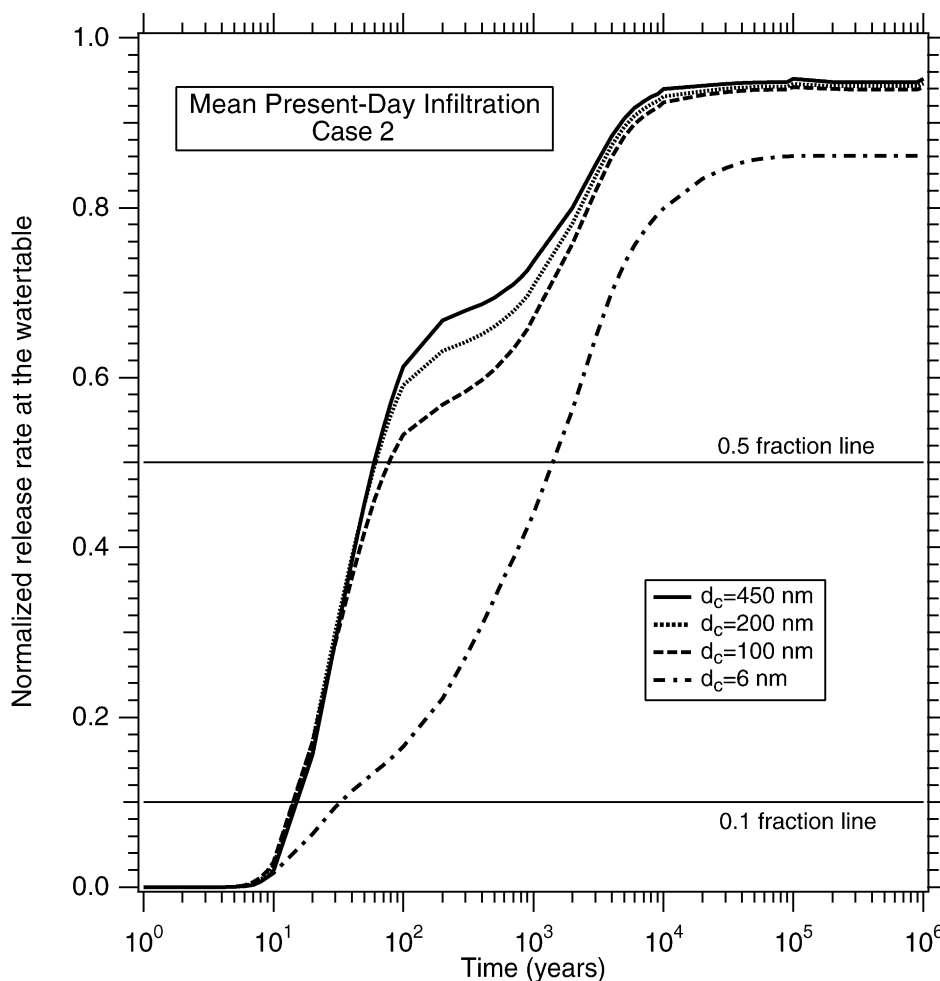
Fig. 3. Normalized release at the water table in Case 2 of colloidal transport for mean present-day infiltration.

the smallest colloid (6 nm) exhibits the slowest breakthrough. This behavior results from a combination of the following factors.

(1) The larger transport velocity of larger colloids, which, by virtue of their size, can only move in the center of pores/fractures where velocities are larger than the average water velocity. In this case, the 450 nm colloid moves at 1.5 times the water velocity (see Table 2).

(2) The inability of larger colloids to penetrate into the matrix from the fractures because of pore size exclusion. Thus, the colloid mass in the fractures is not reduced through matrix diffusion, and practically all of it moves exclusively in the fractures. The 6 nm colloid is capable of diffusing into the matrix, a process that in Fig. 3 manifests itself by the substantially slower breakthrough, the milder rise of the curve, and its lower maximum R value.

4.3.2. Transport of the 6 nm colloid in Case 2

In the study of the radioactive colloid transport, we use the concept of the relative mass fraction X_R^v, defined as

$$X_R^v = \frac{X^v}{X_0^v} = \frac{C^v}{C_0^v} = C_R^v, \quad v \equiv f, m$$

where C is the colloid concentration in the liquid phase ($[ML^{-3}]$), the subscript 0 denotes the value of the subscripted parameter in the water released from the potential repository, and the superscripts f and m denote the fracture and the matrix, respectively. We also use the concept of the relative filtered concentration F_R $[ML^{-3}]$, defined as

$$F_R^v = \frac{F^v}{X_0^v},$$

where F^v is the filtered concentration (i.e., the mass of colloids attached to the rock grains due to physical–chemical filtration) per unit volume.

The areal distribution of the fracture X_R^f of the 6 nm colloid (Co006 in the figures) directly above the TSw–CHn interface (i.e., at the bottom of the TSw, corresponding to the tsw39 layer) is shown in Fig. 4. Note that the distributions at the bottom of the TSw do not correspond to a plan view along a horizontal cross-section, but follow the uneven topography of the bottom of the tsw39 layer. The distance between the bottom of the potential repository to the the TSw–CHn interface varies between about 50 and 150 m (Moridis et al., 2000).

The importance of fractures on the transport of the 6 nm colloid is evident in Fig. 4, which shows that, assuming that the colloid filtration parameters of Case 2 are correct, the colloid concentrations in the fractures of the tsw39 layer is substantial as early as $t = 10$ years and reach a maximum level ($X_R^f = 0.965$) that approaches the release concentration (i.e., $X_R^f = 1$). The reasons for the significant presence (in terms of areal extent and level of concentration) of the 6 nm colloid are that, compared to solutes, (a) diffusion into the matrix is limited because of its relatively large size and pore-size exclusion, (b) filtration in the fracture walls is limited, and (c) the tsw39 layer is above the TSw–CHn interface, where significant filtration occurs. Note that the distribution pattern of X_R^f in Fig. 4
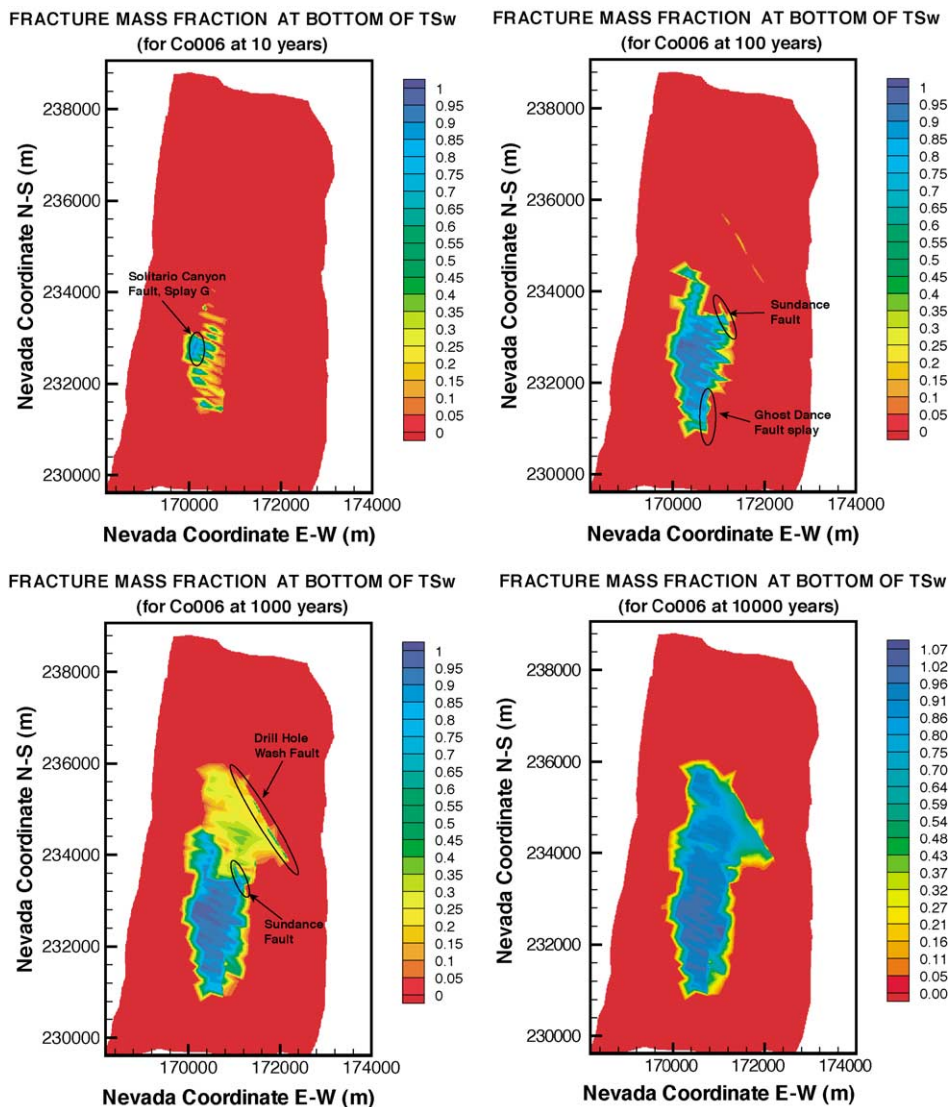
Fig. 4. Distribution of the relative mass fraction X_R^f of the 6 nm colloid in the fractures of the tsw39 layer.

indicates that the colloids accumulate at the TSw−CHn interface and, unable to cross it, move along the sloping interface in an easterly direction.

At $t = 100$ years, the X_R^f in Fig. 4 is significant over a large area and is at its maximum value ($C_R = 1$) over a large portion of this area. The X_R^f distributions at $t = 1000$ years and $t = 10,000$ years follow the same general pattern that is characterized by a progressively increasing affected area (i.e., area with significant X_R values). Note that at $t = 10,000$ years, the maximum $X_R^f = 1.07$ in the tsw39 layer exceeds that in the water released from the

potential repository. This is caused by pore-exclusion (straining) at the TSw−CHn interface, which leads to the accumulation of the 6 nm colloid in the tsw39 layer.

Of particular importance is the X_R^f distribution immediately above the water table shown in Fig. 5. It is remarkable (especially considering its distance from the potential repository) that localized high levels of X_R^f ($= 1.32$, exceeding the release concentration
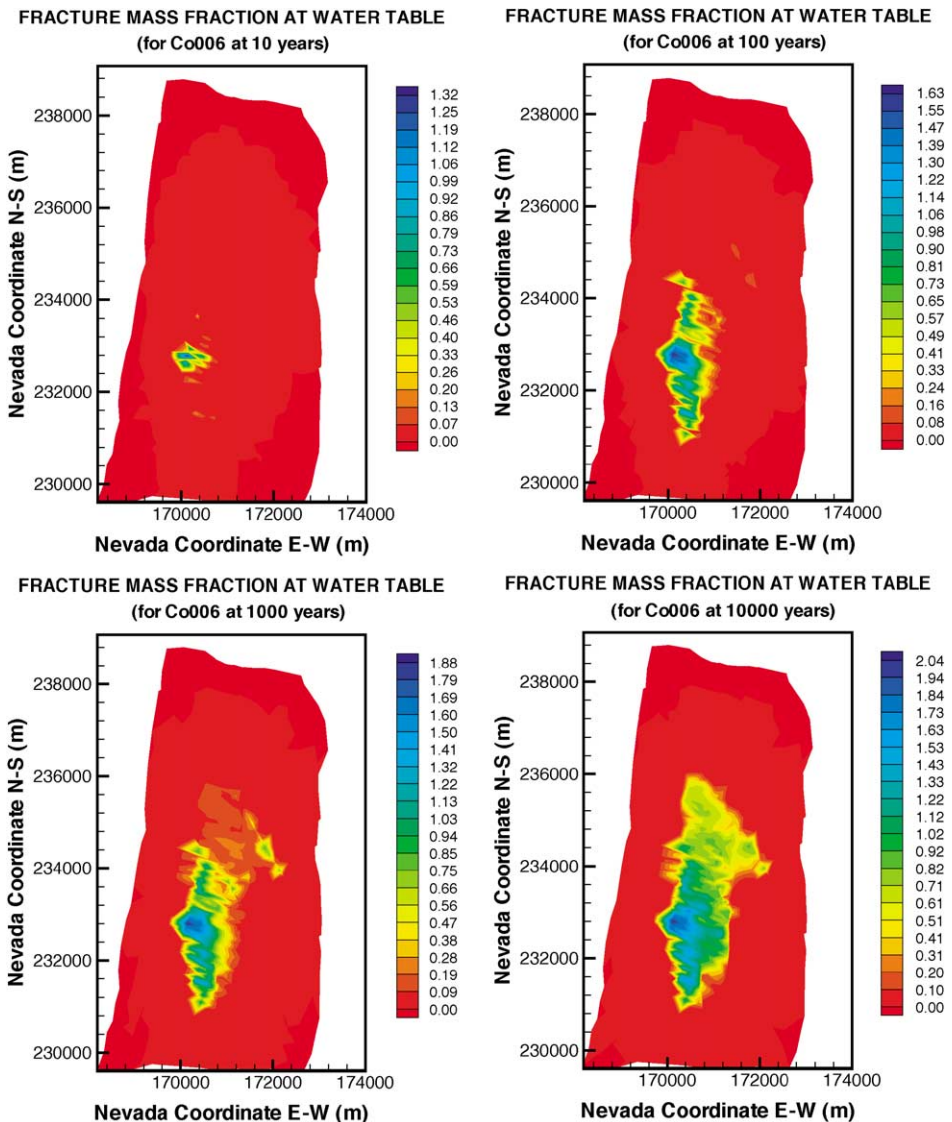

Fig. 5. Distribution of the relative mass fraction X_R^f of the 6 nm colloid in the fractures immediately above the groundwater table.

$X_R^f = 1$), are observed as early as $t = 10$ years. The early appearance results from the fast transport of colloids in the continuous fracture-to-fracture system from the TSw−CHn interface to the water table because of the weak retardation mechansims (previously discussed) related to their size. The areal extent of $X_R^f > 0$ increases consistently over time, as does its peak value, which reaches a level of 2.04 at $t = 10,000$ years, i.e., at this time, the concentration of the 6 nm colloid in the fractures above the water table is more than double that in the water released at the potential repository. The reason for this is that the formation below the water table is treated as porous, resulting in significant straining and accumulation of colloids immediately above the UZ−groundwater interface.

In contrast to Figs. 4 and 5, the X_R^m distribution at the bottom of the TSw (top two images in Fig. 6) begins to show measurable deviations from background at about $t = 1000$ years, and extensive areas of relatively high X_R^m are observed at $t = 10,000$ years. In contrast, X_R^m above the water table (bottom two images in Fig. 6) is even slower to evolve, and shows a substantial signature only at $t = 10,000$ years because of straining (Fig. 5).

The F_R^m distribution of the 6 nm colloid in the tsw39 layer (top two images in Fig. 7) shows very significant F_R^m levels (increasing continuously in areal extent and in magnitude over time) for $t \geq 100$ years. The F_R^m distribution above the water table (bottom two images in Fig. 7) at the same times is slower to evolve and is generally lower. Note that, at both locations, the area of nonzero F_R^m is larger than those of the X_R^f and X_R^m footprints at the same time, and shows the presence of filtered 6 nm colloids at locations with very low X_R^f and X_R^m levels.

In the tsw39 layer, comparison of the F_R^m distribution (Fig. 7) to the X_R^f and the X_R^m distributions (Figs. 4 and 6) reveals intriguing differences: the X_R^m and F_R^m distributions are characterized by an earlier appearance and higher concentrations in the northern part of the potential repository, while the opposite is true for the X_R^f. The reason for the difference in behavior is traced to differences in hydrogeology between the northern and the southern parts of the potential repository at the TSw−CHn interface. Because of straining and limited diffusion and filtration (see earlier discussion), transport of the 6 nm colloid is fast in the fractures. Thus, colloids arrive fast at the interface, which in the southern part is underlain by vitric layers. Although these layers are not as highly fractured as the zeolites in the north, flow through them is matrix-dominated, relatively fast and favors the advective transport indicated in Fig. 4. The effect of the matrix-dominated flow is demonstrated by the magnitude of X_R^f in tsw39, which exceeds 1 due to substantial straining at the underlying interface.

On the other hand, the perched-water model assumed in this study involves flow through permeability barriers (the very reason for the existence of perched-water bodies) in the northern part of the potential repository. The permeability barriers are described as layers in which flow is slow and matrix-dominated. This flow pattern results in the substantial colloid filtration and the F_R^m distribution observed in Fig. 6.

The reason for the lower levels and the delay in the appearance of measurable X_R^m (Fig. 6) is the strong tendency of the colloids to partition into the solid phase of the perched-water bodies through filtration. Note that, while zeolites (with lower access coefficients, see Table 2) are predominant in the underlying layer (see discussion in
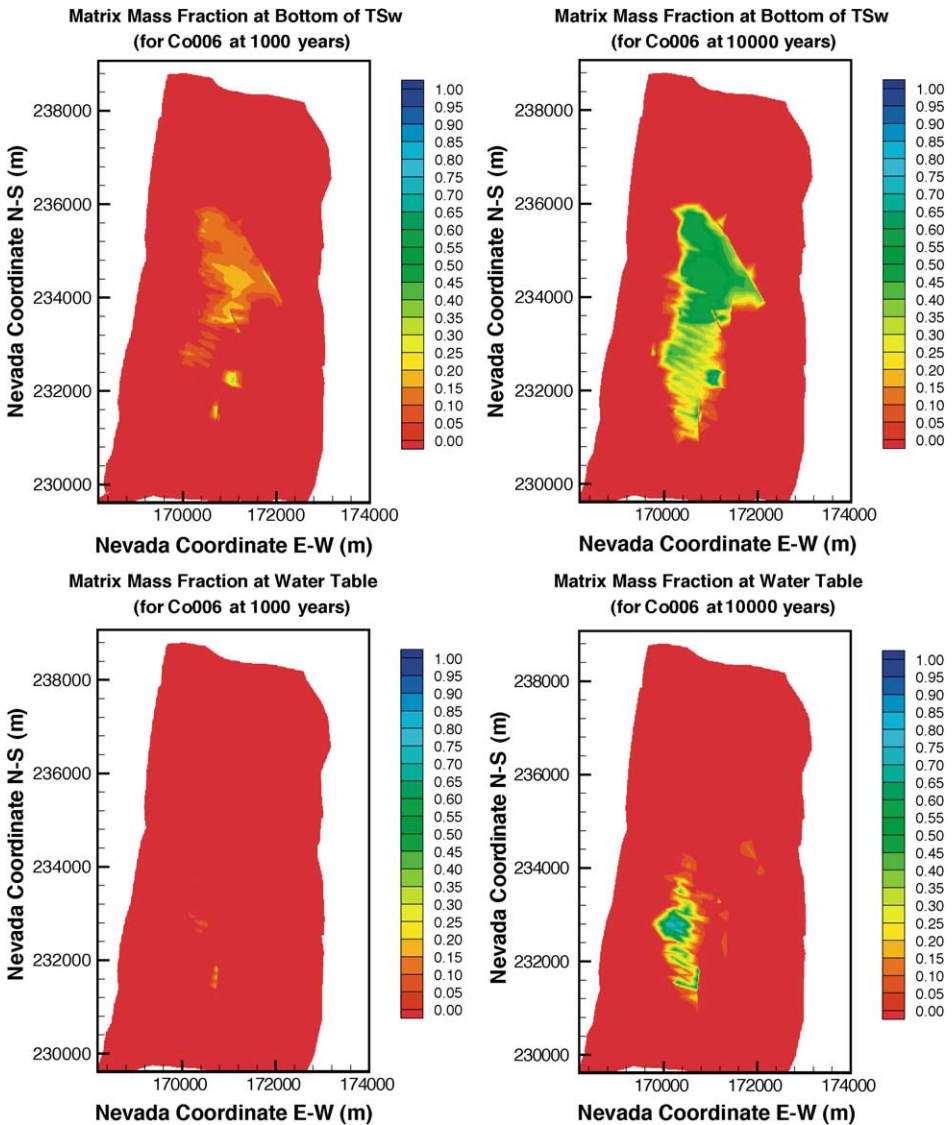
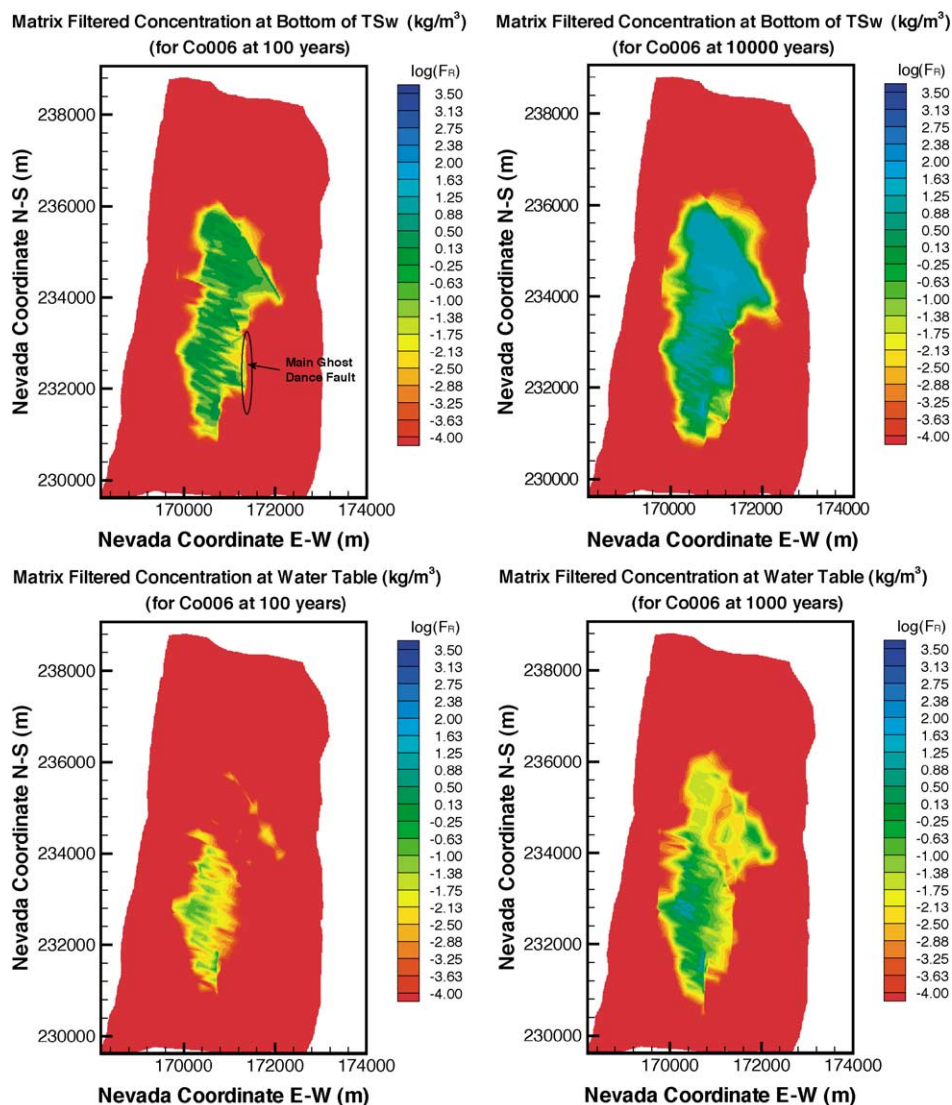Fig. 6. Distribution of the relative mass fraction X_R^m of the 6 nm colloid in the matrix of the tsw39 layer and in the matrix immediately above the water table.

Section 4.3.5), straining is limited in tsw39 because of the extensive fracturing in the zeolites in the northern part of the potential repository and the almost exclusive fracture flow there. The absence of a straining interface is an additional reason for the relatively low levels of X_R^m.

In contrast to the tsw39 layer, the X_R^f, X_R^m and F_R^m distributions at the water table (Figs. 5, 6 and 7) all show that transport occurs predominantly in the southern part of the

Fig. 7. Distribution of the relative filtered concentration F_R^m of the 6 nm colloid in the matrix of the tsw39 layer and in the matrix immediately above the water table.

potential repository. This is attributed to the predominance of flow in the same part (see Section 4.3.5).

4.3.3. Transport of the 450 nm colloid in Case 2

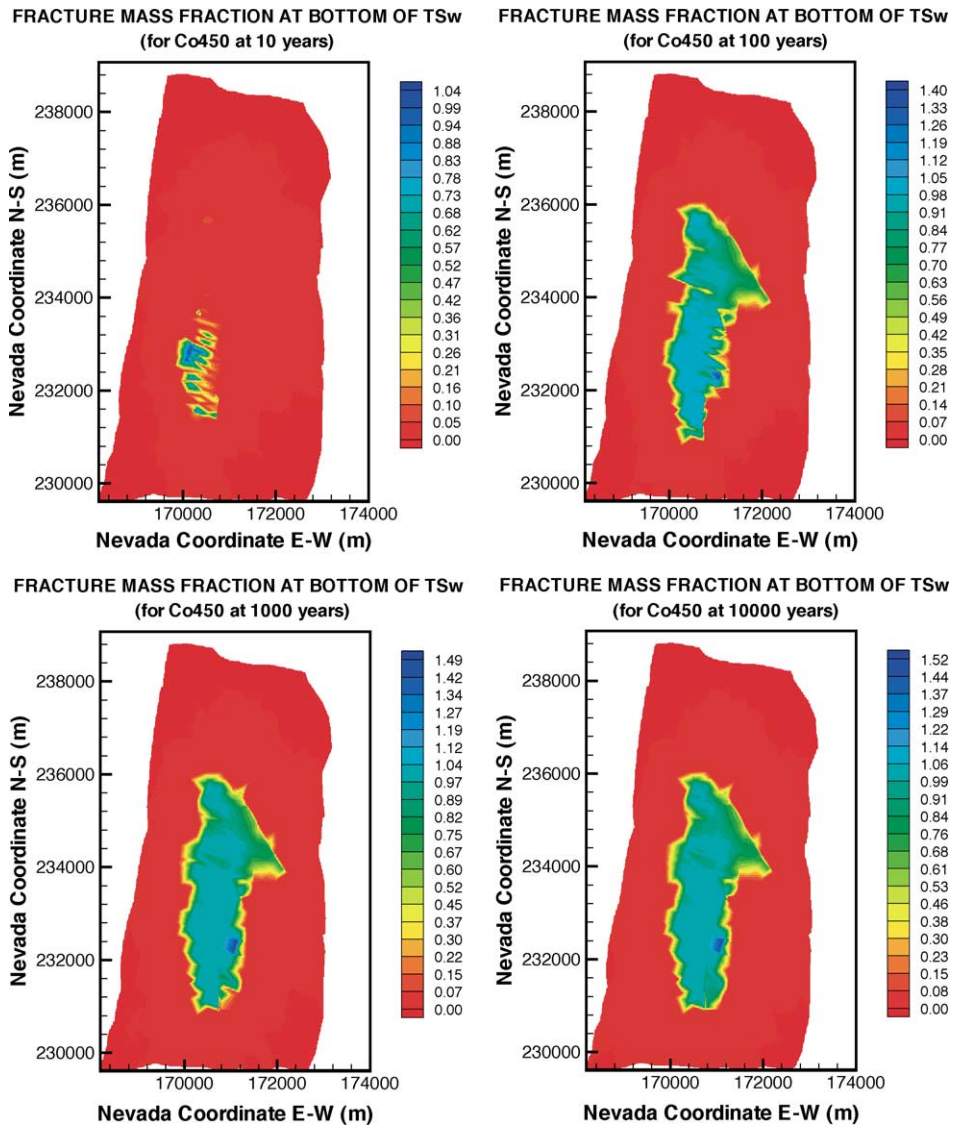The X_R^f distributions of the 450 nm colloid (Co450 in the figures) in the tsw39 and above the water table are shown in Figs. 8 and 9, respectively. The corresponding F_R^m

Fig. 8. Distribution of the relative mass fraction X_R^f of the 450 nm colloid in the fractures of the tsw39 layer.

distributions are shown in Fig. 10, while X_R^m is very low and slow to evolve (Moridis et al., 2000) and is not discussed here. Comparison to the 6 nm colloid results shows that fractures are far more important to the transport of the 450 nm colloid. This is indicated by (a) the larger areal extent and values of X_R^f, and (b) the smaller areal extent and lower values of F_R^m.

At $t = 10$ years, the X_R^f distribution in tsw39 in Fig. 8 has about the same areal extent as the 6 nm colloid, but somewhat higher max$\{X_R^f\} = 1.04$. Substantial differences, however,
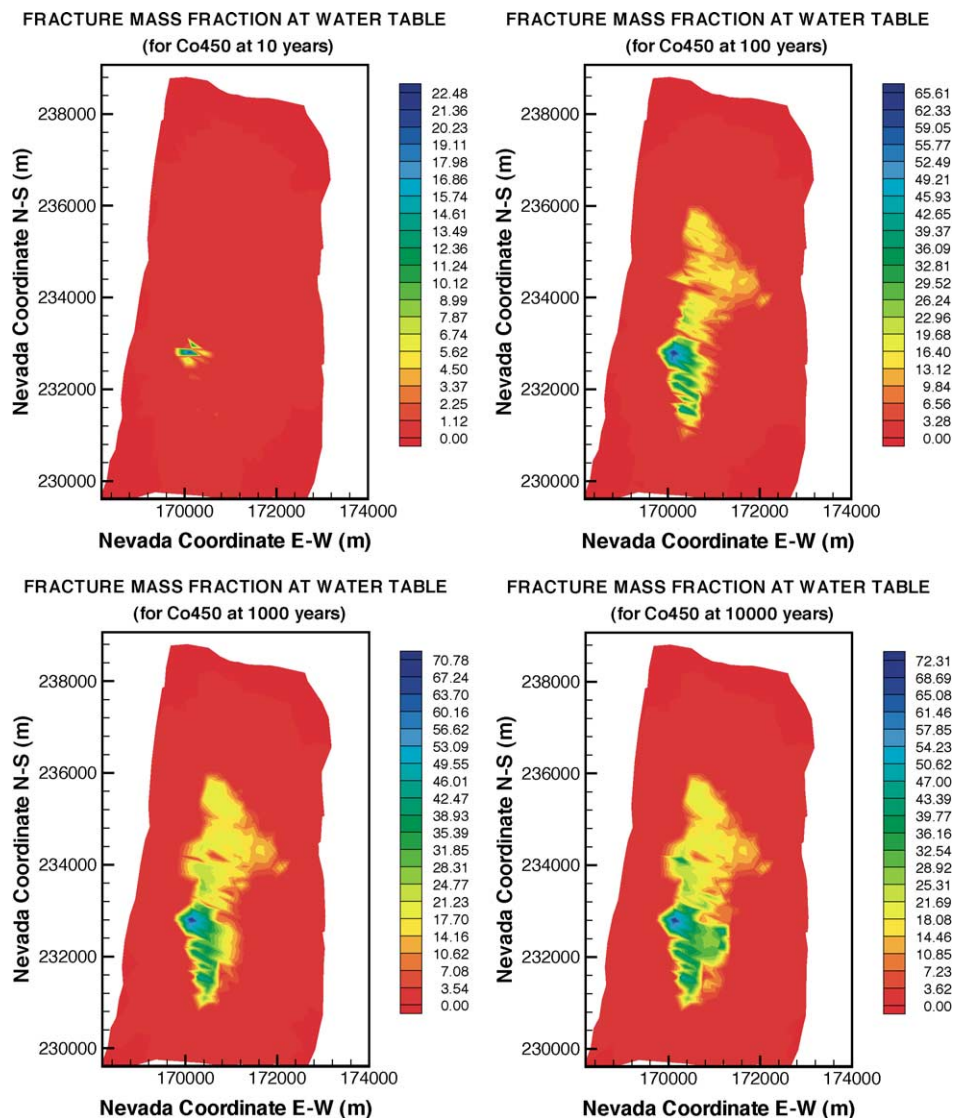
Fig. 9. Distribution of the relative mass fraction X_R^{f} of the 450 nm colloid in the fractures immediately above the groundwater table.

are observed for $t \geq 100$ years, when the distribution pattern indicates contributions from the whole area (at least) of the potential repository, and a much larger footprint than the corresponding 6 nm figure (Fig. 4). Additionally, the max$\{X_R^{\mathrm{f}}\} = 1.40$ exceeds 1 because of accumulation behind the TSw–CHn interface caused by straining. Because of its larger size, the straining is more pronounced in the 450 nm colloid and leads earlier to higher concentrations. The X_R^{f} distribution appears to reach a steady-state areal extent for $t \geq 1000$
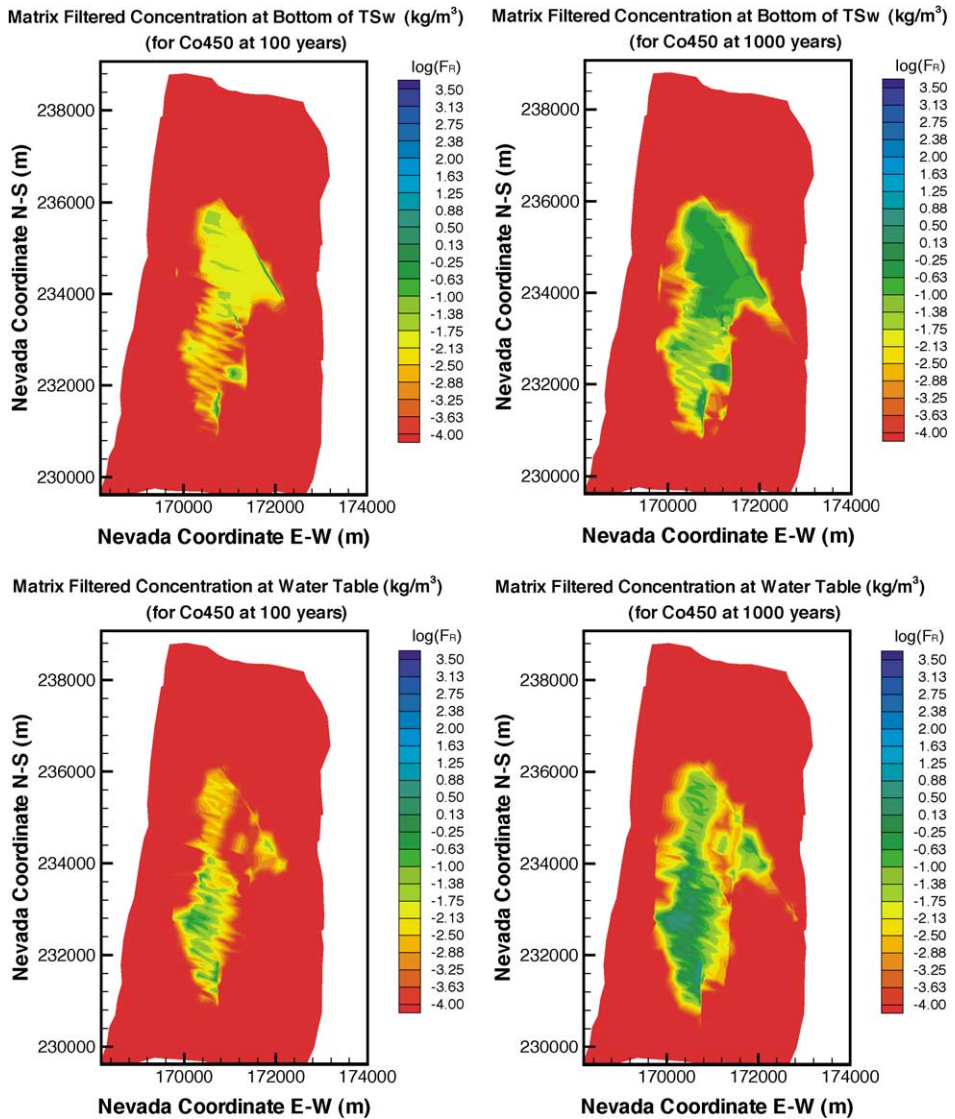
Fig. 10. Distribution of the relative filtered concentration F_R^m of the 450 nm colloid in the matrix of the tsw39 layer and in the matrix immediately above the water table.

years (not substantially larger than that at $t = 100$ years), although max $\{X_R^f\}$ continues to increase (albeit slightly, from 1.49 to 1.52). The obvious conclusion is that transport in the fractures to the tsw39 layer is much faster and more extensive (in areal extent and concentration level) than for the 6 nm colloid because the larger colloid size reduces diffusion into the matrix while increasing straining (thus keeping the colloids in the fractures). The F_R^m distribution in tsw39 (top two images in Fig. 10) is also affected by the

larger colloid size, and is less extended and at lower levels than that of the 6 nm colloid in Fig. 6.

The X_R^f distribution above the water table (Fig. 9) shows a pattern analogous to that for the 6 nm colloid in Fig. 7, but with some significant differences. Early arrivals and very significant localized concentration (max $\{X_R^f\} = 22.5$ of the 450 nm colloid are observed as early as $t = 10$ years. The areal extent and concentration levels increase over time, and reach a max$\{X_R^f\} = 72.3$ at $t = 10,000$ years. These extremely high values are caused by straining at the interface with the underlying groundwater layers. Note that, while this indicates a significant colloid accumulation, it does not necessarily mean clogging and decrease in permeability (at least for a long time) if the concentrations of the colloid waste form are sufficiently low. Compared to the 6 nm colloid, the 450 nm colloid exhibits consistently lower F_R^m values over smaller areas (bottom two images in Fig. 10) for the reasons discussed above.

4.3.4. Transport-controlling geologic features

From the inspection of the transport patterns, it becomes apparent that colloid transport is both dominated and controlled by the faults. A review of the the X_R^f distribution (Figs. 4, 5, 8 and 9) reveals that Splay G of the Solitario Canyon fault (identified in Fig. 4) is the main transport-facilitating feature from below the potential repository through the TSw–CHn interface to the water table. Once contamination reaches the TSw–CHn interface, it moves primarily in an easterly direction, moving with the draining water that hugs the eastward (and downward) sloping low-permeability TSw–CHn interface. The importance of this fault as a transport conduit is indicated by the very early appearance (10 years) of significant levels of colloids at the water table (Figs. 5 and 9).

The Ghost Dance fault splay, identified in Fig. 4, is the next most important transport-facilitating feature in the tsw39 layer, and is also important at the water table. It is remarkable that, though it facilitates downward migration, this fault as modeled appears to act as a barrier to the lateral migration of radionuclides (Figs. 4–10). This is evidenced both in the tsw39 layer and also at the water table.

The Sundance fault and the Drill Hole Wash fault are also important transport-facilitating geologic features, although their contributions begin later. The Drill Hole Wash fault appears to act as a barrier to lateral radionuclide migration across it, while providing pathways for relatively fast transport to the water table. Even at $t = 10,000$ years, very limited migration is observed across it in the tsw39 layer and at the water table (Figs. 4–10).

The main Ghost Dance fault plays a role in transport at later times. This fault (identified in Figs. 2 and 6) acts as a barrier to transport across it while facilitating downward migration into the groundwater. Its presence in the X_R^f and F_R^m distributions is denoted by the sharp contrast between the nonmoving boundary of the concentration front along the fault and the adjacent uncontaminated rock mass. This boundary has the shape of the main Ghost Dance fault (see Fig. 2).

4.3.5. Transport patterns

Of particular interest is the emerging transport pattern, which indicates that colloid transport to the groundwater is faster in the southern part of the potential repository, where

it is also areally concentrated. This appears to be counterintuitive and in conflict with expectations, based on the properties of the layers beneath the potential repository. It would be reasonable to expect that the general area of fastest, largest, and most extensive transport would be in the northern part of the potential repository site, where the highly conductive fractures of the zeolitic CHz layers occur.

The 3-D site-scale simulations indicate that the opposite occurs, i.e., radionuclide transport to the groundwater is significantly slower in the northern part despite the preponderance of the zeolitic CHz units. The relatively large permeability contrast between the matrix and the fractures in the CHz unit does not appear to lead to the expected fast fracture-dominated flow (compared to that in the vitric CHv units in the south) and to a correspondingly fast advective transport.

There are four reasons that explain this transport pattern. The first reason is the infiltration and percolation distributions. A review of the infiltration pattern at the surface, the percolation flux at the repository level, and the percolation flux at the groundwater level (Fig. 11) indicates that they closely reflect the transport patterns in Figs. 4–10. Thus, the water flow pattern dictates the advective transport pattern. In the #1 perched-water model of these studies, the maximum water flow within the footprint of the potential repository is in its southern part.

The presence of the highly conductive (a) Splay G of the Solitario Canyon fault and (b) Ghost Dance fault splay is the second reason (related to the percolation patterns) for the dominance of the southern part of the potential repository as the pathway of transport, despite the vitric CHv layers having fewer fractures (than the overlaying TSw) and acting as porous (rather than fractured) media (with relatively lower water velocities). The permeability of the faults can be as high as hundreds of Darcys (Bodvarsson et al., 1999), i.e., orders of magnitude larger than the adjacent rock. The resulting fast advective transport is the reason for the pattern observed in Figs. 4–10.

This may be further facilitated by the contraction of the areal extent of the vitrified tuffs (the third reason), whose vertical distribution shows a funnel-type structure in the southern part of the potential repository. Thus, as depth from the potential repository increases, an increasing portion of the water flow occurs through the vitrified tuffs, in which flow (and consequently, transport) is fast. Fig. 12 shows the areally diminishing extent (funnel-shaped) of the vitrified tuffs with depth (Bodvarsson et al., 2000). In this figure, the zeolites are indicated by the yellow color in the layers of the CHn and PP hydrogeologic units, while the vitric tuffs are indicated by a purple color. Note also the contrast at the interface of the TSw and CHn units (layers tsw39 and ch1 in Fig. 12).

The fourth reason is the low-permeability zones at the TSw–CHn interface in the northern part of the potential repository in the #1 perched water model (Wu et al., 2000). These zones are barriers to drainage and lead to low water velocities and perched water bodies. Colloids move slowly through the perched water before reaching the underlying highly permeable zeolite fractures, hence the delay in transport.

Note that the importance of faults and perched water bodies in transport is directly dependent on the underlying geologic and perched water conceptual models. It is reasonable to expect that changing geologic and perched water models may lead to different results, given the sensitivity of transport to these geologic features.
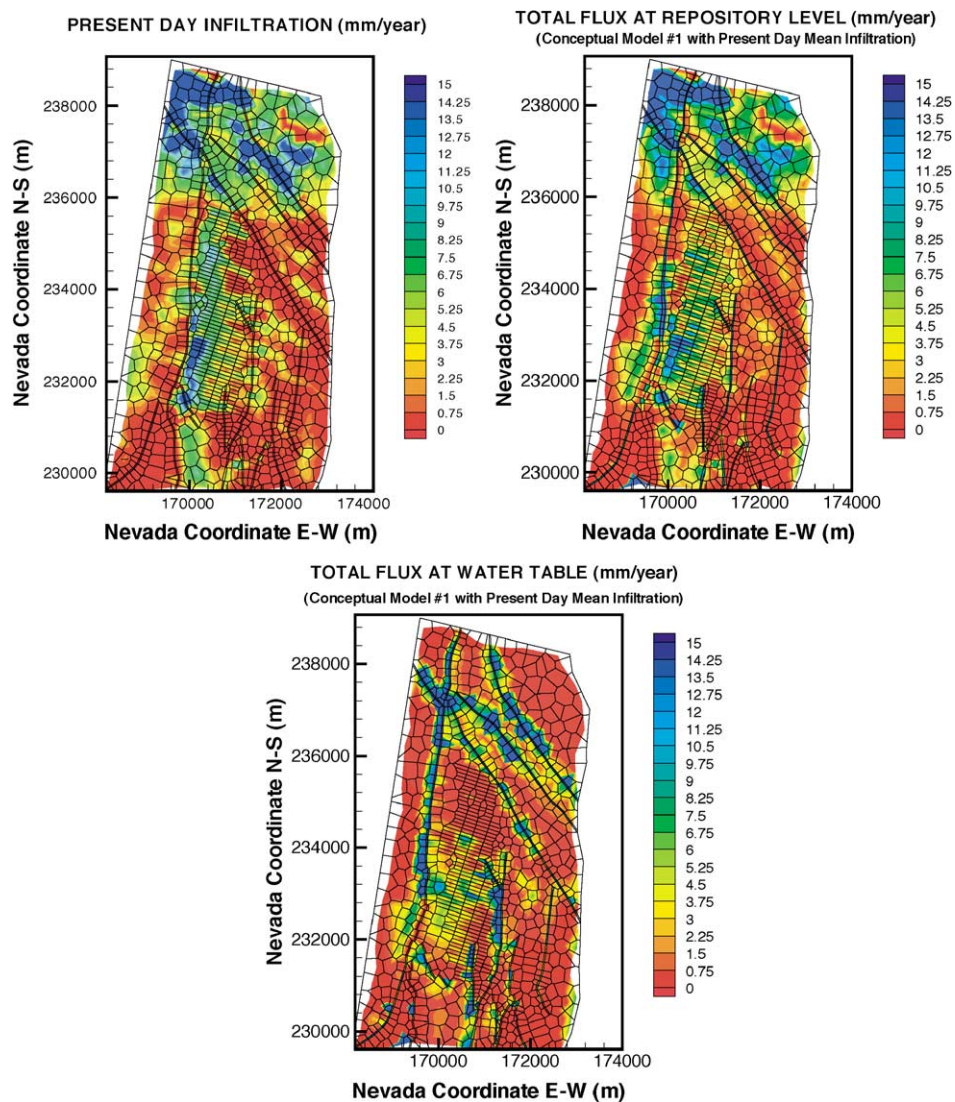
Fig. 11. Mean present-day infiltration rates at the surface and percolation fluxes at the potential repository level and at the water table level (Wu et al., 2000).

4.4. Colloid transport in Case 3

The change in the magnitude of the reverse kinetic filtration coefficient κ^- (as a fraction of κ^+) has a rather dramatic effect on colloid transport (Fig. 13). This case involves slower declogging and results in a breakthrough that occurs at a time about three orders of magnitude larger than that of Case 2 (see Fig. 3). Thus, t_{10} is 12,000 years for the 450, 200, and 100 nm colloids, and infinity for the 6 nm colloid; t_{50} is infinity for all
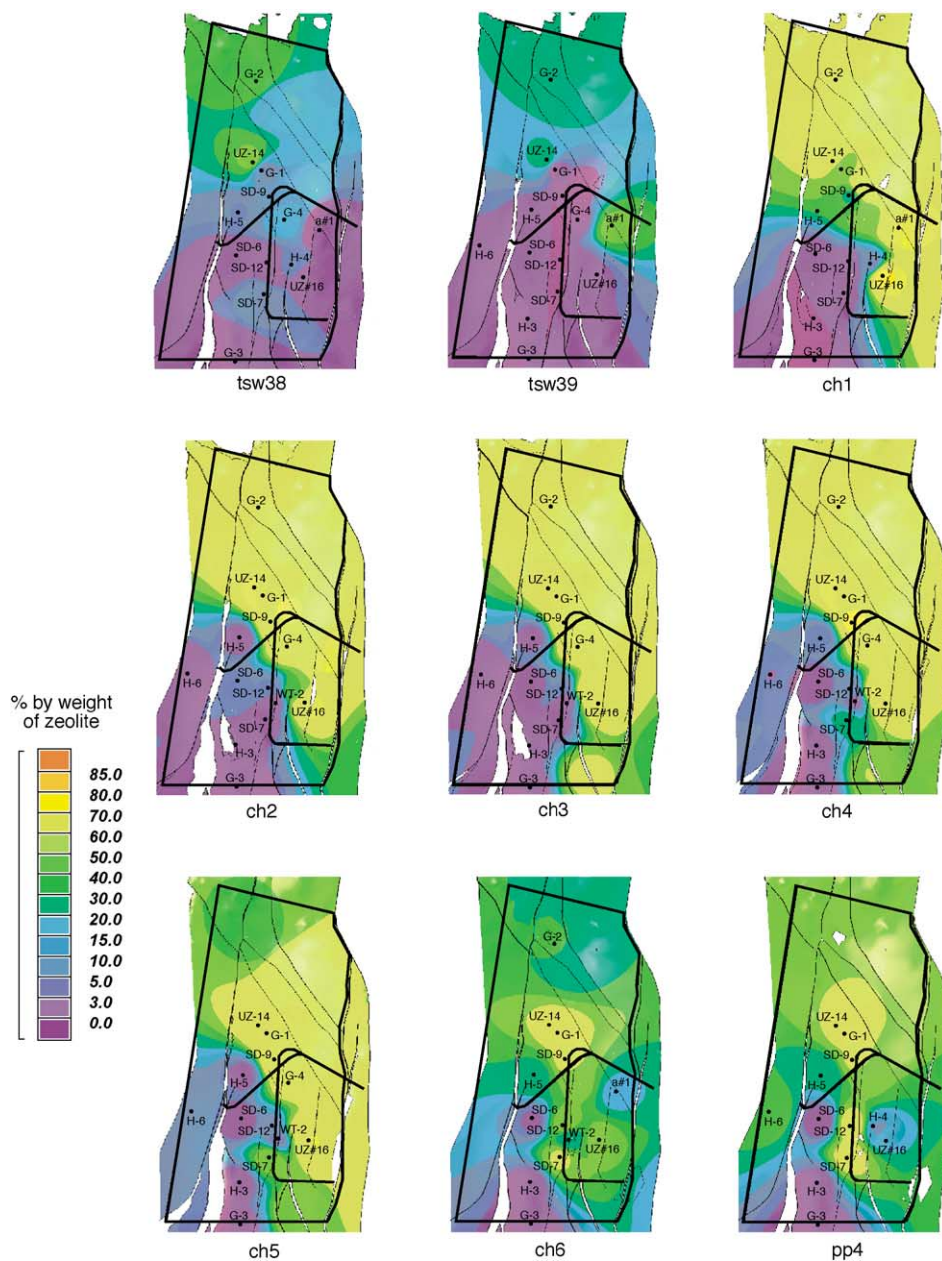
Fig. 12. Mineralogy model plots of % zeolites (Bodvarsson et al., 2000). Vitric tuffs are indicated by the purple color.
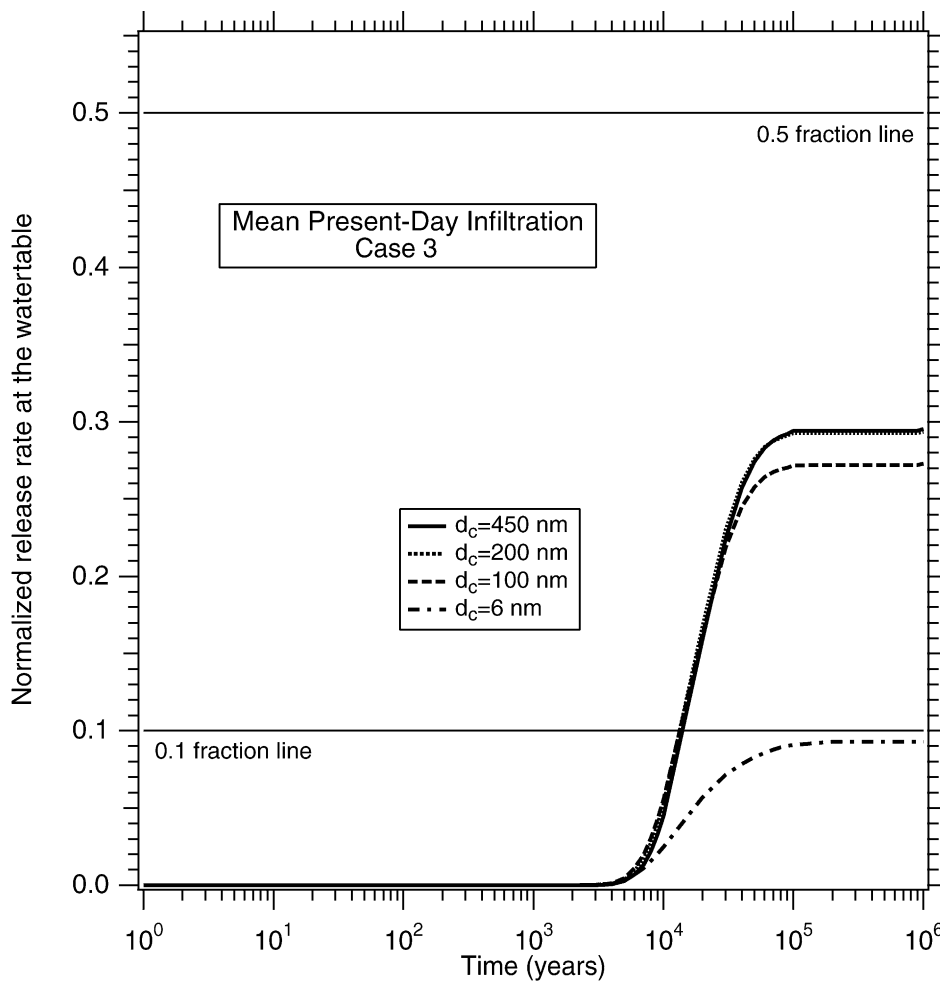
Fig. 13. Normalized release at the water table in Case 3 of colloidal transport for mean present-day infiltration.

colloids because the maximum normalized release rate at the water table never exceeds 0.3.

For the reasons discussed in Section 3, the larger three colloids reach the groundwater first. The 6 nm colloid reaches the groundwater slightly later, but it has a substantially different R curve, with a maximum value (plateau) of only about $R = 0.097$, i.e., about one-third that for the 450 nm colloid. This stems from both larger diffusion into the matrix and the resulting slower transport, which allows radioactive decay to decrease the colloid mass.

4.5. Colloid transport in Case 4

Setting the fracture filtration properties equal to those of the matrix results leads to the transport scenario depicted in Fig. 14. The effect of limited diffusion on transport (because
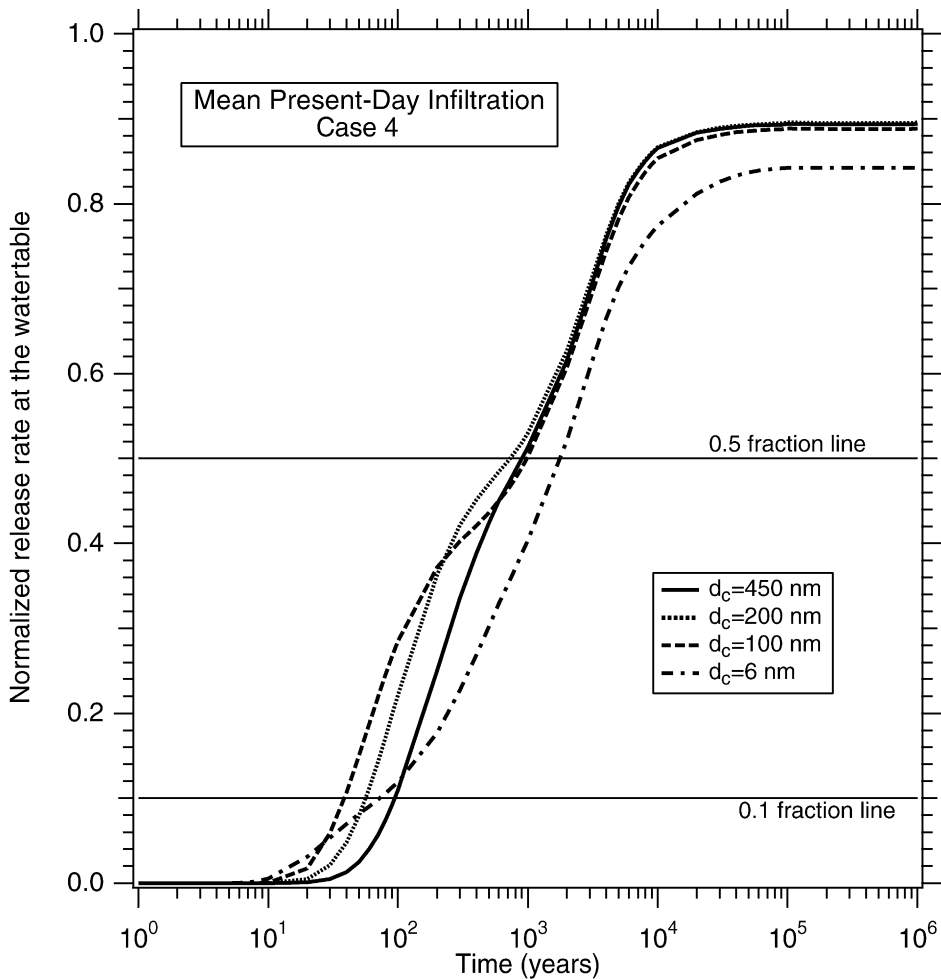
Fig. 14. Normalized release at the water table in Case 4 of colloidal transport for mean present-day infiltration.

of straining and filtration) becomes more obvious in this case. Thus, the 6 nm colloids are the first to reach the groundwater, the 450 nm are the last, and the arrival times of the rest increase with their diameter.

The reason for this case was to obtain a measure of the relative importance of the fractures in UZ colloid transport. The t_{50} of the three larger colloids is about 1000 years, and 2000 years for the smallest colloid. Given that the significant difference between Figs. 3 and 14 is due solely to assigning matrix filtration properties to only 1% of the pore volume of the fractures, the significant retardation of the colloids indicates the importance of fractures and their relative contribution to the total colloid transport through the UZ system.

4.6. The importance of colloid diffusion

In this section, we investigate the effect on transport of an alternative conceptual model that assumes no diffusion. For the conditions of Case 2 (see Section 4.2), the breakthrough curves for no diffusion in Fig. 15 are quite similar to the ones obtained when colloid diffusion is considered (see Fig. 3). This was expected because of (a) the limited colloid diffusion owing to their large size, and (b) size exclusion (straining) effects at the interfaces of different layers further limit entry through diffusion into the matrix (especially for larger colloids).
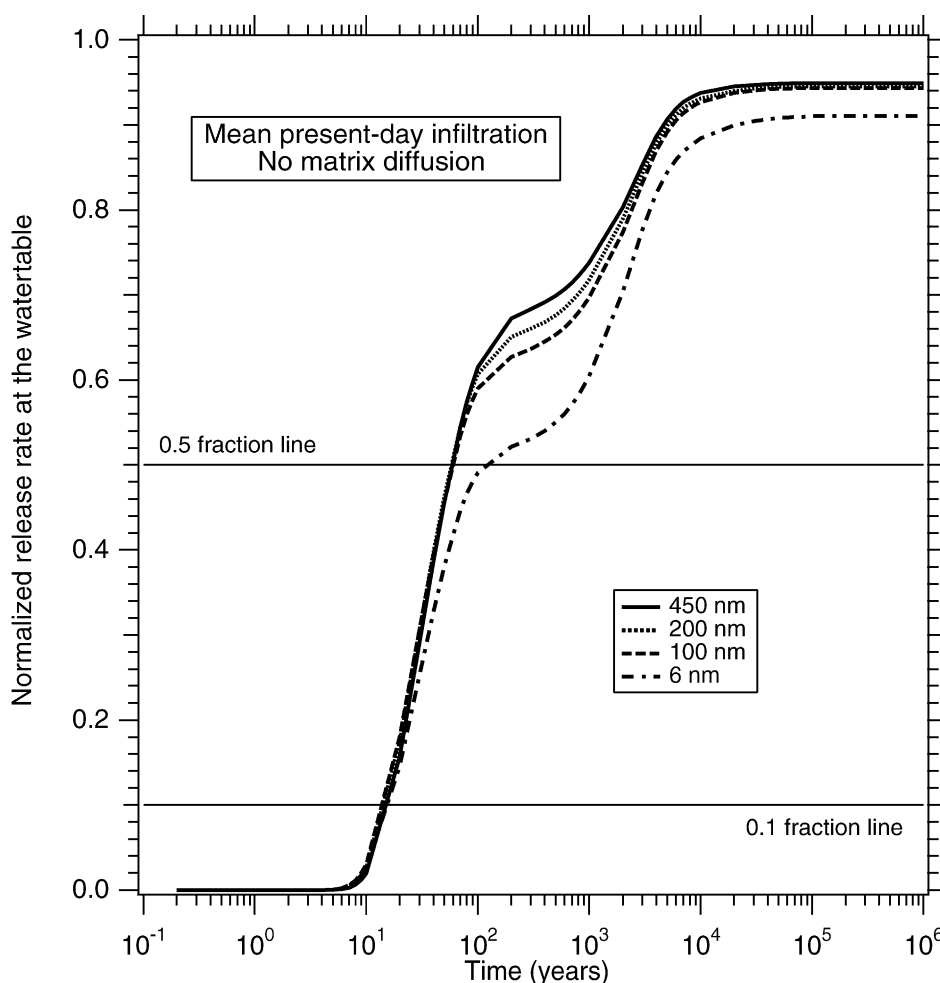

Fig. 15. Normalized relative releases of radioactive colloids at the water table for the no-diffusion alternative model (mean present-day infiltration, #1 perched water model, Case 2 conditions).

The early portions (up to 70 years) of the breakthrough curves for the 450, 200 and 100 nm colloids are identical, indicating the same filtration behavior and the limited importance of diffusion in larger colloids. Comparison of the curves in Figs. 3 and 15 shows the increasing importance of diffusion as the colloid size decreases. Thus, including diffusion leads to limited retardation of the transport of the 100 nm colloid, but the effect is more pronounced in the case of the 6 nm colloid. Its t_{10} and t_{50} are reduced from 300 and 1500 years to 15 and 100 years, respectively.

Thus, diffusion does not appear to play a significant role in the retardation of larger colloids. Its effect, however, becomes increasingly important for a decreasing colloid size.

5. Summary and conclusions

The following conclusions can be drawn from this study.

(1) The study of colloid transport in the UZ at YM is hampered by significant knowledge gaps both in the areas of basic science and reliable field data. The current state of knowledge does not allow reliable predictions, and bracketing the solution is hard because of the extreme variations in the range of possible answers.

(2) Under the #1 perched-water model, radionuclide transport from the bottom of the potential repository to the water table is both dominated and controlled by the faults. These provide fast pathways to downward migration to the water table, but also limit lateral transport past them.

(3) Radioactive colloids from the potential repository move faster and reach the water table earlier and over a larger area in the southern part of the potential repository. There are four reasons for this transport pattern.

(a) Infiltration and percolation distributions. The water flow pattern dictates the advective transport pattern. In the #1 perched-water model of these studies, the maximum water flow within the footprint of the potential repository is in its southern part.

(b) The presence of the highly conductive Splay G of the Solitario Canyon fault and of the Ghost Dance fault splay. Additionally, the Sundance fault, the Drill Hole Wash fault, and the main Ghost Dance fault are transport-facilitating geologic features. Of these, the Drill Hole Wash fault and the main Ghost Dance fault act as barriers to the northward and eastward radionuclide movement, while providing pathways for relatively fast transport to the water table.

(c) The contraction of the areal extent of the vitrified tuffs, forcing an increasing portion of the water flow through the vitrified tuffs, in which flow and transport are fast.

(d) The low-permeability zones at the TSw−CHn interface in the northern part of the potential repository in the #1 perched-water model.

(4) For a mean present-day infiltration and a given kinetic clogging (forward filtration) coefficient κ^+, the transport of radioactive true colloids is strongly influenced by the kinetic declogging (reverse filtering) coefficient κ^-. When no declogging is allowed, no colloids reach the groundwater. Low values of κ^- (i.e., slow declogging) lead to long travel times to the water table (and thus significant retardation). For $\kappa^-/\kappa^+ = 0.1$, t_{10} is 12,000 years for the 450, 200, and 100 nm colloids, and infinity for the 6 nm colloid; t_{50} is

infinity for all colloids because the maximum normalized release rate at the water table never exceeds 0.3.

Large values of κ^- lead to a dramatically different behavior, with very fast travel times of the radioactive colloids to the water table. For $\kappa^-/\kappa^+ = 100$, t_{10} is 15 years for the 450, 200 and 100 nm colloids, and 30 years for the 6 nm colloids. The t_{50} is about 60 years for the 450 and 200 nm colloids, about 80 years for the 100 nm colloid, and 1200 years for the 6 nm colloid. The extreme sensitivity of colloid filtration (deposition) on κ^- and the dearth of any representative information on its value in the various UZ hydrogeologic units underline the need for attention to this subject.

(5) For a given κ^-, colloid size has a significant effect on transport. Given that fractures are the main transport conduit in the UZ of YM, the inability of larger colloids to diffuse into the matrix because of smaller D_0 values and straining result in faster transport to the groundwater. Smaller colloidal particles can diffuse easier into the matrix, and their transport is thus retarded.

(6) Straining at the interfaces of different hydrogeologic layers leads to colloid concentrations immediately above the interface that can be significantly higher than that in the water released from the potential repository. This phenomenon is more pronounced in larger colloids.

(7) The importance of diffusion as a retardation mechanism increases with decreasing colloid size, but appears to be minimal in large colloids.

Acknowledgements

References

Ahlers, C.F., Finsterle, S., Bodvarsson, G.S., 1999. Characterization and prediction of sub-surface pneumatic response at Yucca Mountain, Nevada. J. Contam. Hydrol. 38 (1–3), 47–68.

Bandurraga, T.M., Bodvarsson, G.S., 1999. Calibrating hydrogeologic parameters for the 3D site-scale unsaturated zone model of Yucca Mountain, Nevada. J. Contam. Hydrol. 38 (1–3), 25–46.

Bates, J.K., Bradley, J.P., Teetsov, A., Bradley, C.R., ten Brink, M.B., 1992. Colloid formation during waste form reaction: implications for nuclear waste disposal. Science 256, 649–651.

Birkholzer, J., Li, G., Tsang, C.-F., Tsang, Y., 1999. Modeling studies and analysis of seepage into drifts at Yucca Mountain. J. Contam. Hydrol. 38 (1–3), 349–384.

Bodvarsson, G.S., Boyle, W., Patterson, R., Williams, D., 1999. Overview of scientific investigations at Yucca Mountain—the potential repository for high-level nuclear waste. J. Contam. Hydrol. 38 (1–3), 3–24.

Bodvarsson, G.S., Ahlers, C.F., Cushey, M., Dove, F.H., Finsterle, S.A., Haukwa, C.B., Hinds, J., Ho, C.K., Houseworth, J., Hu, Q., Liu, H.H., Pendleton, M., Sonnenthal, E.L., Unger, A.J., Wang, J.S.Y., Wilson, M., Wu, Y.-S., 2000. Unsaturated zone flow and transport process model report. Civilian Radioactive Waste Management System, Management and Operations (CRWMS M&O), Las Vegas, Nevada.

Bowen, B.D., Epstein, N., 1979. Fine particle deposition in smooth parallel-plate channels. J. Colloid Interface Sci. 72, 81–97.

Buddemeier, R.W., Hunt, J.R., 1988. Transport of colloidal contaminants in groundwater: radionuclide migration at the Nevada Test Site. Appl. Geochem. 3, 535–548.

Buesch, D.C., Spengler, R.W., Moyer, T.C., Geslin, J.K., 1995. Revised stratigraphic nomenclature and macroscopic identification of lithostratigraphic units of the Paintbrush group exposed at Yucca Mountain, Nevada. USGS Open-File Report 94-469, U.S. Geological Survey, Denver, CO.

Clayton, R., 2000. Geologic framework model (GFM3.1) analysis model report. Report MDL-NBS-GS-000002 Rev. 00. CRWMS M&O, Las Vegas, NV.

Conca, J., 2000. Unsaturated zone and saturated zone transport properties. Report ANL-NBS-HS-000019 Rev. 00. CRWMS M&O, Las Vegas, NV.

Conca, J.L., Wright, J., 1990. Diffusion coefficients in gravel under unsaturated conditions. Water Resour. Res. 26 (5), 1055–1066.

Çorapçioglu, M.Y., Abboud, N.M., Haridas, A., 1987. Governing equations for particle transport in porous media. In: Bear, J., Çorapçioglu, M.Y. (Eds.), Advances in Transport Phenomena in Porous Media, Applied Sciences Series 128, Series E. Martinus Nijhoff Publishers, Dordrecht, pp. 269–342.

DeHoog, F.R., Knight, J.H., Stokes, A.N., 1982. An improved method for numerical inversion of Laplace transforms. SIAM J. Sci. Statist. Comput. 3 (3), 357–366.

de Marsily, G., 1986. Quantitative Hydrogeology: Groundwater Hydrology for Engineers. Academic Press, Orlando, FL.

DOE (U.S. Department of Energy), 1998. Viability assessment of a repository at Yucca Mountain, Vol. 3, Total system performance assessment. Report DOE/RW-0508, DOE, Washington, DC.

Doughty, C., 1999. Investigation of conceptual and numerical approaches for evaluating moisture, gas, chemical and heat transport in fractured unsaturated rock. J. Contam. Hydrol. 38 (1–3), 69–106.

Dyer, J.R., Voegele, M.D., 1996. High-level radioactive waste management in the United States, background and status. In: Witherspoon, P.A. (Ed.), Geological Problems in Radioactive Waste Isolation. Report LBNL-38915. Lawrence Berkeley National Laboratory, Berkeley, CA, pp. 259–270.

Electric Power Research Institute (EPRI), 1999. Colloids in saturated and partially-saturated porous media: Approaches to the treatment of colloids in Yucca Mountain total system performance assessment. Report TR-112135, EPRI, Palo Alto, CA.

Farrell, J., Reinhard, M., 1994. Desorption of halogenated organics from model solids, sediments, and soil under unsaturated conditions: 2. Kinetics. Environ. Sci. Technol. 28 (1), 63–72.

Grathwohl, P., 1998. Diffusion in Natural Porous Media: Contaminant Transport, Sorption Desorption and Dissolution Kinetics. Kluwer Academic Publishing, Boston, MA.

Harvey, R.W., Garabedian, S.P., 1991. Use of colloid filtration theory in modeling movement of bacteria through a contaminated sandy aquifer. Environ. Sci. Technol. 25 (1), 178–185.

Haukwa, C., Wu, Y.-S., Bodvarsson, G.S., 1999. Thermal loading studies using the Yucca Mountain unsaturated zone model. J. Contam. Hydrol. 38 (1–3), 25–46.

Herzig, J.P., Leclerc, D.M., Le Goff, P., 1970. Flow of suspension through porous media. Ind. Eng. Chem. Res. 62 (5), 129–157.

Hevesi, J., Flint, L., 2000. Simulation of net infiltration for modern and potential future climate. U.S. Geological Survey Report ANL-NBS-GS-000008.

Hinds, J., Pan, L., 2000. Development of numerical grids for UZ flow and transport modeling. Report ANL-NBS-HS-000015 Rev. 00. CRWMS M&O, Las Vegas, NV.

Hu, Q., Brusseau, M.L., 1995. The effect of solute size on transport in structured porous media. Water Resour. Res. 31 (7), 1637–1646.

Ibaraki, M., Sudicky, E.A., 1995. Colloid-facilitated contaminant transport in discretely fractured media: 1. Numerical formulation and sensitivity analysis. Water Resour. Res. 31 (12), 2945–2960.

Jacobsen, O.H., Moldrup, P., Larsen, C., Konnerup, L., Peterson, L.W., 1997. Particle transport in macropores of undisturbed soil columns. J. Hydrol. 196, 185–203.

James, S.C., Chrysikopoulos, C.V., 1999. Transport of polydisperse colloid suspensions in a single fracture. Water Resour. Res. 35 (3), 707–718.

Kersting, A.B., Efurd, D.W., Finnegan, D.L., Rokop, D.J., Smith, D.K., Thompson, J.L., 1999. Migration of plutonium in ground water at the Nevada Test Site. Nature 397, 56–59.

Lide, D.R., 1992. CRC Handbook of Chemistry and Physics, 73rd ed. CRC Press, Boca Raton, FL.

Liu, H.H., Doughty, C., Bodvarsson, G.S., 1998. An active fracture model for unsaturated flow and transport in fractured rocks. Water Resour. Res. 34 (10), 2633–2646.

Liu, H.H., Ahlers, C.F., Cushey, M.A., 2000. Analysis of hydrologic properties. Report ANL-NBS-HS-000002 Rev. 00. CRWMS M&O, Las Vegas, NV.

McCarthy, J.F., Zachara, J.M., 1989. Subsurface transport of contaminants. Environ. Sci. Technol. 23 (5), 496–502.

McGraw, M.A., 2000. UZ colloid transport model. Report ANL-NBS-HS-000028 Rev. 00. CRWMS M&O, Las Vegas, NV.

McKenzie, D.G., 1999. Input transmittal for enhanced design alternative (EDA) II repository layout for 10 cm/s ventilation plan. Report ACC: MOL.19990409.0102. CRWMS M&O, Las Vegas, NV.

Montazer, P., Wilson, W.E., 1984. Conceptual hydrologic model of flow in the unsaturated zone, Yucca Mountain, Nevada. Resources Investigations Report 84-4355. U.S. Geological Survey, Denver, CO.

Moridis, G., Wu, Y., Pruess, K., 1999. EOS9nT: a TOUGH2 Module for the Simulation of Flow and Solute/Colloid Transport. Report LBNL-42351. Lawrence Berkeley National Laboratory, Berkeley, CA.

Moridis, G., Hu, Q., Wu, Y., Bodvarsson, K., 2000. Modeling Studies of Radionuclide Transport in the Unsaturated Zone of Yucca Mountain, Nevada. Report LBNL-42351. Lawrence Berkeley National Laboratory, Berkeley, CA.

Pruess, K., 1991. TOUGH2: A General Purpose Numerical Simulator for Multiphase Fluid and Heat Flow. Report LBL-29400, UC-251. Lawrence Berkeley National Laboratory, Berkeley, CA.

Smith, P.A., Degueldre, C., 1993. Colloid-facilitated transport of radionuclides through fractured media. J. Contam. Hydrol. 13, 143–166.

Sonnenthal, E.L., Bodvarsson, G.S., 1999. Constraints on the hydrology of the unsaturated zone at Yucca Mountain, NV from three-dimensional models of chloride and strontium geochemistry. J. Contam. Hydrol. 38 (1–3), 107–156.

van de Weerd, H., Leijnse, A., 1997. Assessment of the effect of kinetics on colloid facilitated radionuclide transport in porous media. J. Contam. Hydrol. 26, 245–256.

Vilks, P., Bachinski, D.B., 1996. Colloid and suspended particle migration experiments in a granite fracture. J. Contam. Hydrol. 21, 269–279.

Vilks, P., Frost, L.H., Bachinski, D.B., 1997. Field-Scale colloid migration experiments in a granite fracture. J. Contam. Hydrol. 26, 203–214.

Wan, J., Tokunaga, T.K., 1997. Film straining of colloids in unsaturated porous media: conceptual model and experimental testing. Environ. Sci. Technol. 31 (8), 2413–2420.

Wang, J.S.Y., Trautz, R.C., Cook, P.J., Finsterle, S., James, A.L., Birkholzer, J., 1999. Field tests and model analyses of seepage into drift. J. Contam. Hydrol. 38 (1–3), 323–348.

Wu, Y.S., Ritcey, A.C., Bodvarsson, G.S., 1999a. A modeling study of perched water phenomena in the unsaturated zone at Yucca Mountain. J. Contam. Hydrol. 38 (1–3), 157–184.

Wu, Y.S., Haukwa, C., Bodvarsson, G.S., 1999b. A site-scale model for fluid and heat flow in the unsaturated zone of Yucca Mountain, Nevada. J. Contam. Hydrol. 38 (1–3), 185–216.

Wu, Y.S., Liu, J., Xu, T., Haukwa, C., Zhang, W., Liu, H.H., Ahlers, C.F., 2000. UZ flow models and submodels. Report MDL-NBS-HS-000006 Rev. 00. CRWMS M&O, Las Vegas, NV.

Yao, K.M., Habibian, M.T., O'Melia, C.R., 1971. A model for colloid filtration. Environ. Sci. Technol. 11, 1105–1112.